GRACE-FO radiation pressure modelling for accurate density and crosswind retrieval

Hładczuk, N. A.; van den IJssel, J.; Kodikara, T.; Siemes, C.; Visser, P.

DOI
10.1016/j.asr.2023.12.059

Publication date
2024

Document Version
Final published version

Published in
Advances in Space Research

Citation (APA)
Hładczuk, N. A., van den IJssel, J., Kodikara, T., Siemes, C., & Visser, P. (2024). GRACE-FO radiation pressure modelling for accurate density and crosswind retrieval. *Advances in Space Research*, *73*(5), 2355-2373. https://doi.org/10.1016/j.asr.2023.12.059

Available online at www.sciencedirect.com

ScienceDirect

Advances in Space Research 73 (2024) 2355–2373

ADVANCES IN SPACE RESEARCH
(a COSPAR publication)

www.elsevier.com/locate/asr

GRACE-FO radiation pressure modelling for accurate density and crosswind retrieval

N.A. Hładczuk [a,*], J. van den IJssel [a], T. Kodikara [b], C. Siemes [a], P. Visser [a]

[a] *Department of Astrodynamics and Space Missions, Faculty of Aerospace Engineering, Delft University of Technology, Kluyverweg 1, Delft 2629 HS, Netherlands*

[b] *Institute for Solar-Terrestrial Physics, German Aerospace Center, Kalkhorstweg 53, Neustrelitz 17235, Germany*

Received 31 October 2023; received in revised form 24 December 2023; accepted 28 December 2023
Available online 2 January 2024

Abstract

Uncertainties in radiation pressure modelling play a significant role in the thermospheric density and crosswind observations derived from the GRACE-FO accelerometer, especially during low solar activity. Under such conditions, the radiation pressure acceleration matches the magnitude of the aerodynamic acceleration along the track and exceeds it in the cross-track direction. The GRACE-FO mission has been operating for several years at such high altitudes during both low and rising solar activity, providing a perfect opportunity to study the effects of radiation pressure. This research uses ray tracing based on a high-fidelity satellite geometry model to calculate the radiation pressure acceleration. We numerically fine-tuned the coefficients describing the thermo-optical surface properties to obtain more accurate radiation pressure accelerations than those specified in the GRACE-FO mission manual. We also used in situ temperature measurements from thermistors on the solar arrays to model the satellite's thermal emission. These temperature measurements allowed a realistic setup of the thermal model, extended by the parameter describing the efficiency of the solar cells, and reproduced the acceleration of the thermal emission with an accuracy of RMS 0.148 nms^{-2}. The combination of the updated thermal model and the fine-tuning of the surface coefficients improved the accuracy of the crosswind acceleration to an RMS of 0.55 nms^{-2}, compared to an RMS of 4.22 nms^{-2} when using panel models and instantaneous thermal radiation. We compared the observed crosswind with two models: HWM14 and TIE-GCM. While both models capture most of the salient features of the observed crosswind, HWM14 shows particularly good agreement at high latitudes. Compared to the previously employed radiation pressure model, the crosswind observations have been improved in low and mid-latitudes, especially during periods of higher solar activity. Since the effect of radiation pressure is most significant in the crosswind direction, the effect on density was small compared to previously published datasets.

Keywords: Thermosphere; Neutral mass density; Neutral winds; Thermal emission; Radiation pressure; GRACE-FO

---

1. Introduction

The Gravity Recovery And Climate Experiment Follow-On (GRACE-FO) mission's primary objective is measuring Earth's time-variable gravity field to deduce mass changes with high precision. GRACE-FO was launched in May 2018 and remains operational until today. The mission consists of two identical satellites flying in a near-polar orbit around Earth at an initial altitude of approximately 510km (Kornfeld et al., 2019), and a current altitude of 500km, as of September 2023. The satellites share the same orbital plane with a nominal along-track separation of 220 ±50km, continuously measuring the relative distance between each other. GRACE-FO extends the scientific

---

* Corresponding author.
E-mail addresses: N.A.Hladczuk@tudelft.nl (N.A. Hładczuk), J.A.A.vandenIJssel@tudelft.nl (J. van den IJssel), Timothy.Kodikara@dlr.de (T. Kodikara), C.Siemes@tudelft.nl (C. Siemes), P.N.A.M.Visser@tudelft.nl (P. Visser).

https://doi.org/10.1016/j.asr.2023.12.059
0273-1177/© 2023 COSPAR. Published by Elsevier B.V.

legacy of its predecessor, the GRACE mission (Tapley et al., 2004). Both missions share the same principal design features, however, a laser-ranging interferometer was added to GRACE-FO as a technology demonstration. The GRACE-FO satellites are equipped with a dual-frequency GPS receiver, star trackers and high-precision accelerometers. These instruments allow for measuring the non-gravitational forces acting on the satellites, from which we deduce neutral mass density and crosswind observations (Doornbos, 2011). Shortly after launch, the GRACE-D accelerometer data degraded, and its measurements were replaced by a synthetic data transplant (Landerer et al. (2020),Harvey et al. (2022)). Therefore, this article focuses solely on the better-performing GRACE-C satellite. This study will enhance the radiation pressure and thermal emission models for GRACE-FO to obtain a more accurate neutral mass density and crosswind dataset, which complements earlier published data from the CHAMP, GRACE, GOCE, and Swarm missions (Siemes et al., 2023). Producing thermosphere density and crosswind observations relies on the aerodynamic acceleration obtained by subtracting the radiation pressure from the calibrated acceleration. Therefore, uncertainties in the radiation pressure modelling propagate directly into the density and crosswind datasets. This effect is particularly profound for GRACE-FO altitude during low solar activity. In such conditions, the radiation pressure matches the magnitude of the aerodynamic acceleration in the along-track direction and even surpasses it in the cross-track. Since the GRACE-FO mission has been operating for several years at such high altitudes during both low (2018–2021) and rising solar activity, it provides a perfect opportunity to study the effects of radiation pressure. The foundation of the non-gravitational force modelling is the definition of the satellite geometry model. Its complexity varies, starting from the straightforward approach based on a satellite panel model. Such a model implies using a limited number of flat panels to characterise the satellite's outer geometry (Bettadpur, 2012). Replacing commonly used panel models with high-fidelity geometries for aerodynamic modelling has increased the accuracy and consistency of thermospheric density and crosswind data (March et al., 2019). To take advantage of the high-fidelity geometry models for the radiation pressure modelling, we must first augment them with thermo-optical surface properties. These models can then be used in ray-tracing simulations to determine the radiation pressure force coefficients. Ray-tracing is an efficient method for modelling the momentum exchange between each ray and satellite surface. It can cope with complex satellite shapes while accounting for self-shadowing and multiple reflections. One way to implement the ray-tracing simulation is to perform calculations for each position along the orbit independently (Kenneally and Schaub, 2020). Regardless of its simple implementation, this method requires high computational resources and is, therefore, not a feasible option to process the entire GRACE-FO mission data. In this study, we perform the ray-tracing simulations in advance and store the results as a lookup table. This approach is very similar to the one proposed by Klinkrad et al. (1991) and applied by Doornbos et al. (2002). It has been later adopted by different groups working on GNSS precise orbit determination (Ziebart (2004),Li et al. (2018), Bhattarai et al. (2022)).

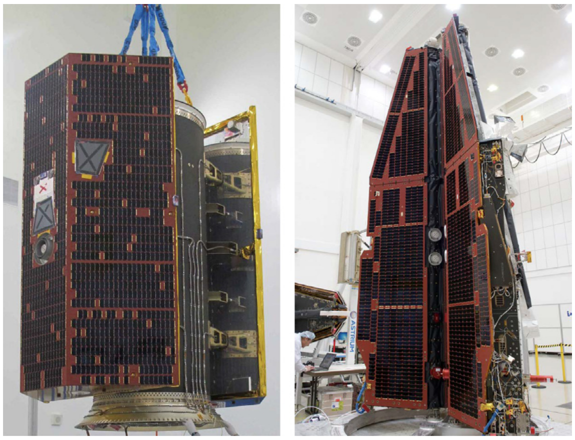

(a) GRACE-FO[1] (b) Swarm[2]

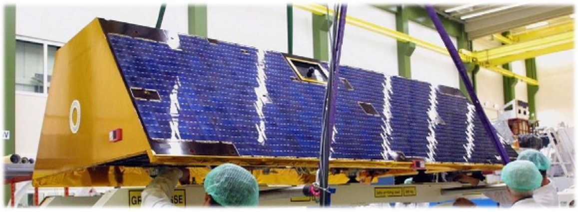

(c) GRACE[3]

Fig. 1. Comparison between the solar arrays of GRACE-FO[1], Swarm[2], and GRACE[3].

Thermal acceleration typically accounts for one-fourth of total cross-track radiation pressure acceleration. A common approach to model thermal emission relies on the assumption of simple instantaneous heat reradiation and no heat conduction between and through elements (Montenbruck et al. (2015),Vielberg and Kusche (2020)). The state-of-the-art thermal models reproduce the temperatures of the outer panels, taking into account their thermal inertia (Wöske et al. (2019),Wang et al. (2023)). In this scenario, the satellite surface heats up by absorbing incoming radiation and cools down by emitting radiation. This process can be implemented using thermal model control parameters such as internal heat generation, heat capacity of the panels, and conductance towards the inner parts.

Within the last few years, significant progress has been made in the field of radiation pressure and thermal emission modelling. Nevertheless, specific gaps can still

---

[1] airbus.com/en/newsroom/press-releases/2017-05-grace-fo-satellites-get-an-earful accessed on 03/10/2023.

[2] esa.int/ESA_Multimedia/Images/2012/02/Swarm_constellation_in_IABG_cleanroom2 accessed on 03/10/2023.

[3] wetteronline.de/wetternews/astro accessed on 19/10/2023.

be identified, such as insufficient knowledge of the thermo-optical properties of the satellite material. According to the GRACE-FO Level-1 Data Product User Handbook (Ying et al., 2019), the reflection coefficients do not differ between GRACE and GRACE-FO. However, there are numerous design differences between the two missions. One of them is the solar arrays illustrated in Fig. 1, which were upgraded from silicon ones used on GRACE to triple-junction panels (GaAs), previously qualified for the Swarm mission and characterised by higher absorption of visible light (Kornfeld et al., 2019). The need to update the thermo-optical surface properties for GRACE-FO has already been addressed by Siemes et al. (2023). However, the proposed set of reflection coefficients was selected empirically based on the visual inspection of the accelerometer data and prelaunch satellite photos. The same publication introduced the thermal inertia model, with the heat capacity and conductivity of the panels based on the theoretical values of the respective panels. However, it ignored that part of the radiation absorbed by the solar arrays converts to electricity, commonly referred to as the electric efficiency of the solar arrays.

This research aims to provide new insights into selecting the thermo-optical surface coefficients for GRACE-FO using numerical optimisation. Additionally, we tuned a thermal model to accurately match the actual surface temperature measurements obtained from the GRACE-FO thermistors. To achieve even more realistic thermal behaviour, we introduced the efficiency of the solar arrays (Duan and Hugentobler, 2022), which was not the case in previously published GRACE-FO data (Siemes et al., 2023).

This paper is organised as follows. Section 2 describes the input data and models used in this study. Section 3 elaborates on methodology in the context of thermal emission and radiation pressure modelling. We summarise the results in Section 4, comprising the thermal modelling and surface reflection coefficients fine-tuning, the effect on the cross-track acceleration and updated crosswind and density datasets. Finally, Section 5 provides conclusions and an outlook on future work.

2. Data and models

2.1. GRACE-FO data

This study utilises Level 1 GRACE-FO data publicly available via FTP ftp://isdcftp.gfz-potsdam.de, specifically, the acceleration, attitude, position, velocity, thruster, satellite mass, and accelerometer temperature data. We rely on the higher temporal resolution of the Level 1A accelerometer data to enable easier removal of the acceleration due to thruster activations. Additionally, we use the NRLMSISE-00 model (Picone et al., 2002a) to model the atmospheric composition and temperature. Wind in the direction of the satellite's x-axis is accounted for by the HWM07 model (Drob et al., 2008). To measure the non-gravitational accelerations, the GRACE-FO satellites were equipped with the SuperSTAR-FO accelerometers, an advanced version of the ones used previously for the GRACE mission (Christophe et al., 2015). The accelerometer noise level in the along-track is about 0.1 nms^{-2}, whereas the cross-track measurements are about 10 times less precise by design.

2.2. Thermistor data

This study took advantage of in situ measurements from GRACE-FO thermistors provided by NASA Jet Propulsion Laboratory (JPL) to select realistic thermal model control parameters. Thermistors monitor the temperature on the inner and outer satellite's surfaces in several locations. Sensors on the solar arrays were particularly useful since they provided the most representative temperature readings due to their external location. Numerous other thermistors were mounted on the inner side of the panels or below insulating foils, making their measurements unsuitable for thermal analysis.

Fig. 2 shows the location of the temperature sensors on GRACE-FO solar arrays and their registered temperature measurements for the year 2020. The horizontal and vertical axis of the temperature data correspond to time and the argument of latitude. Each column denotes a single orbital revolution, where 0° is the ascending equator crossing, 90° indicates the northernmost point of the orbit, 180° marks the descending equator crossing and 270° is the southernmost points of the orbit. The 360° point marks the start of the next revolution at the equator.

We compared the temperature readings from thermistors on the same panel to examine thermal gradients across the surface. Thermistors located closer to the satellite's rear register at maximum 10K higher temperatures, in comparison to the central sensors (Fig. 3). We consider such temperature differences small enough to assume a uniform temperature over the whole panel area.

2.3. Geometry models

Accurate aerodynamic and radiation pressure modelling requires detailed satellite geometries rather than simple panel models. Such geometries were already created for multiple low Earth orbit satellites such as CHAMP, Swarm, GOCE and GRACE (March et al., 2019). This article relies on the high-fidelity GRACE-FO geometry (Fig. 4), first published by Siemes et al. (2023). This model, which consists of 23,746 facets, acted as a baseline for deriving aerodynamic coefficients and calculating radiation pressure accelerations. For the radiation pressure modelling, different surface properties were assigned to individual materials, defining absorption and reflection coefficients for both visible and infrared parts of the spectrum. We initially selected the thermo-optical surface properties from the GRACE-FO Level-1 Data Product User Handbook (Ying et al., 2019). For materials that remained unspecified in the documentation, we used the properties specified by Fortescue et al. (2011).

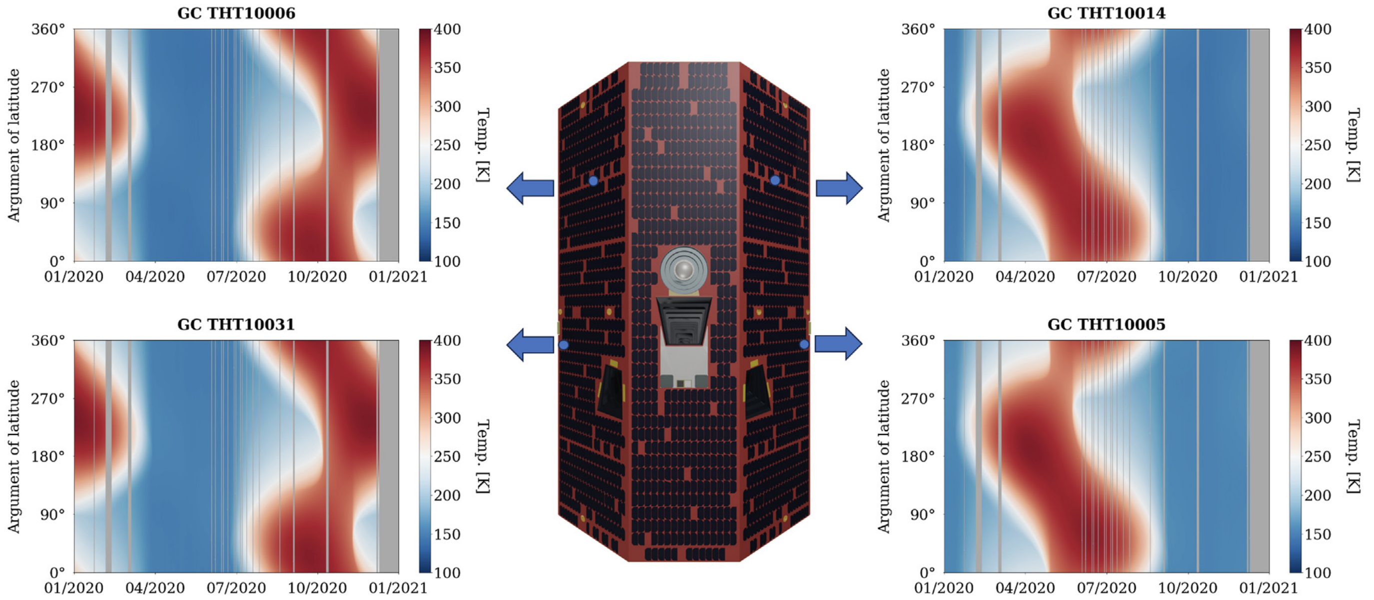

Fig. 2. GRACE-FO top view with the thermistors' location on solar arrays (indicated by blue dots) and corresponding temperature measurements. The thermistors' IDs are indicated in the title (e.g., THT10014). The grey colour indicates data gaps. (For interpretation of the references to colour in this figure legend, the reader is referred to the web version of this article.)

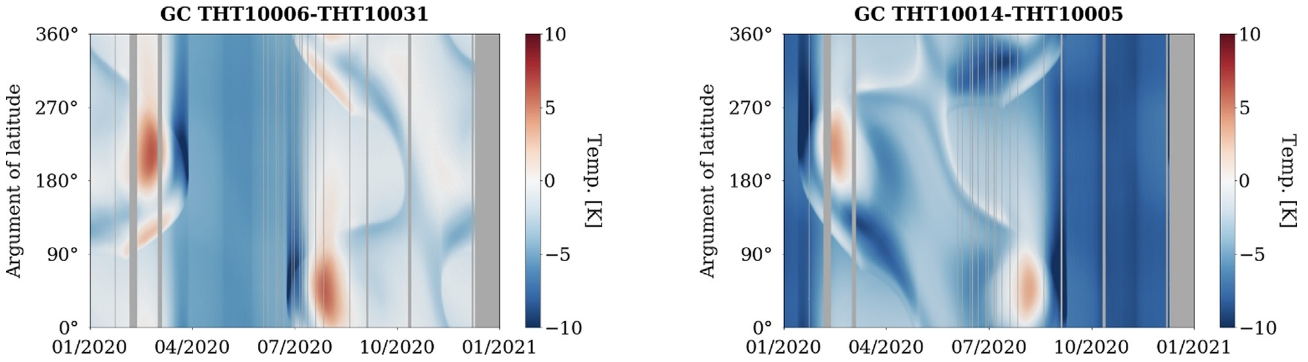

Fig. 3. Comparison between the temperature measurements from thermistors on the same solar array. The thermistors' IDs are indicated in the title (e.g., THT10014).

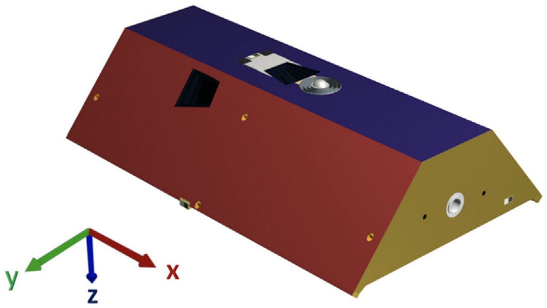

Fig. 4. Rendered GRACE-FO geometry model used as an input for the ray-tracing algorithm. Colours correspond to individual material properties. The axes are aligned with the satellite reference frame.

2.4. TIE-GCM

We use the physics-based thermosphere-ionosphere-electrodynamics general circulation model (TIE-GCM; Richmond et al., 1992) to validate the crosswind data. It is a time-dependent three-dimensional numerical model of the coupled thermosphere and ionosphere system. This work is based on TIE-GCM version 2.0 (2016) and resolves the system at a horizontal resolution of 2.5°x2.5° in latitude and longitude and a vertical resolution of 0.25 scale height. The exact configuration of the model used in this study along with the simulated data are provided in Kodikara (2023).

2.5. HWM14

The Horizontal Wind Model is an empirical model of the horizontal neutral wind in the upper thermosphere. The model consisted primarily of data from two NASA satellites (Explorer 55 and Dynamics Explorer 2), ground-based incoherent scatter radar and Fabry–Perot optical interferometers (FPI). As described in subSection 2.1 we used the HWM07 model (Drob et al., 2008) to account for wind in the direction of the satellite's x-axis. However, for the comparison with observation data, we used the most recent model version HWM14, which was updated with ground-based 630nm FPI measurements in the equatorial and polar regions, as well as cross-track winds from the Gravity Field and Steady State Ocean Circulation Explorer (GOCE) satellite (Drob et al., 2015). The updates in HWM14 fill important gaps in both latitude and local time coverage and provide an improved specification of the upper atmospheric tides and general circulation patterns. Currently, the model does not account for solar activity dependence. The variations with geomagnetic activity are specified via the Ap index.

2.6. DTM2020

The Drag Temperature Model (DTM2020) is a semi-empirical model providing information on the Earth's thermosphere temperature, density and compositions (Bruinsma and Boniface, 2021). This study used the operational version of the model to assess the neutral mass density datasets. The DTM2020 is driven by the F10.7 and Kp indices for solar and geomagnetic activity. The core of the model is CHAMP, GOCE and GRACE accelerometer data together with GNSS measurements from the Swarm-A satellite. In addition, very accurate laser tracking data from the Stella satellite have been incorporated.

2.7. NRLMSISE-00 model

NRLMSISE-00 is a semi-empirical atmosphere model based on a wide range of data, including mass spectrometer and incoherent scatter radar data. It is also based on neutral mass density datasets derived from accelerometer measurements and orbital decay of objects that flew during the 1960s and 1980s (Picone et al., 2002b). We point out that the NRLMSISE-00 model is independent of the density datasets produced after 2000. The model provides the thermosphere density, temperature, and composition. We used the latter two as input for density and crosswind data processing and the first for comparing to the density observations.

3. Methodology

For satellites, such as GRACE-FO, where the accelerometer placement coincides with the satellite's centre of mass, the aerodynamic acceleration vector $\boldsymbol{a}_{\mathrm{aero}}$ can be obtained by subtracting the radiation pressure acceleration, $\boldsymbol{a}_{\mathrm{rp}}$, and thermal acceleration, $\boldsymbol{a}_{\mathrm{the}}$, from the calibrated accelerometer acceleration, $\boldsymbol{a}_{\mathrm{cal}}$:

$$\boldsymbol{a}_{\mathrm{aero}} = \boldsymbol{a}_{\mathrm{cal}} - \boldsymbol{a}_{\mathrm{rp}} - \boldsymbol{a}_{\mathrm{the}}. \tag{1}$$

The total radiation pressure acceleration is the sum

$$\boldsymbol{a}_{\mathrm{rp}} = \boldsymbol{a}_{\mathrm{srp}} + \boldsymbol{a}_{\mathrm{ir}} + \boldsymbol{a}_{\mathrm{alb}}, \tag{2}$$

where $\boldsymbol{a}_{\mathrm{srp}}$ stands for the solar radiation pressure acceleration, and $\boldsymbol{a}_{\mathrm{ir}}$ and $\boldsymbol{a}_{\mathrm{alb}}$ are Earth's infrared radiation and albedo, respectively.

Fig. 4 shows the satellite body-fixed reference frame. During nominal operations, the satellite x-axis is oriented in the anti-flight and in-flight directions for the leading and trailing satellites, respectively. The y-axis corresponds to the direction perpendicular to the orbital plane (cross-track), and the z-axis to the nadir direction (toward Earth). Since the satellite's x-axis is approximately aligned with the flight direction, it captures most of the drag signal. Therefore, we use the x-component of the aerodynamic acceleration, $a_{aero,x}$, to derive the neutral mass density:

$$\rho = \frac{2\,m\,a_{\mathrm{aero},x}}{C_{\mathrm{aero},x}\,V_{rel}^2}. \tag{3}$$

Here, m denotes the satellite mass, $C_{aero,x}$ is the x-component of the aerodynamic coefficient vector intrinsically multiplied by the reference area, and V_{rel} is the velocity relative to the atmosphere. Neutral mass density and crosswinds retrieval rely on accurate aerodynamic acceleration estimation, formerly derived using the radiation pressure acceleration (Eq. (1)). This reliance creates a dependency between the radiation pressure modelling uncertainty and the density and crosswind quality. The impact of radiation pressure modelling errors is most prominent at altitudes above 450km during low solar activity. In such conditions, the along-track component of radiation pressure acceleration matches or even surpasses the magnitude of the aerodynamic acceleration. This effect was already quantified for the Swarm satellites (van den IJssel et al., 2020), as well as GRACE (Wöske et al., 2019), and GRACE-FO, in which case the radiation pressure acceleration doubled the magnitude of aerodynamic acceleration during deep solar minimum in 2018–2020 (Siemes et al., 2023).

The crosswind retrieval is based on the iterative algorithm proposed by Doornbos et al. (2010). In the cross-track direction, the aerodynamic acceleration signal is much smaller (Fig. 5), resulting in a strong impact of radiation pressure modelling errors on the crosswind estimate.

This chapter presents the methodology, starting from the radiation pressure modelling approach in Section 3.1, complemented by thermo-optical surface coefficients fine-tuning in Section 3.3, and the thermal emission modelling description in Section 3.2.

3.1. Radiation pressure modelling

Radiation pressure acceleration acting on the satellite can be calculated as

$$\boldsymbol{a}_{\mathrm{ext}}(\alpha,\beta) = \frac{P_{\mathrm{ext}}(\alpha,\beta)}{m}\boldsymbol{C}_{\mathrm{w}}(\alpha,\beta), \tag{4}$$

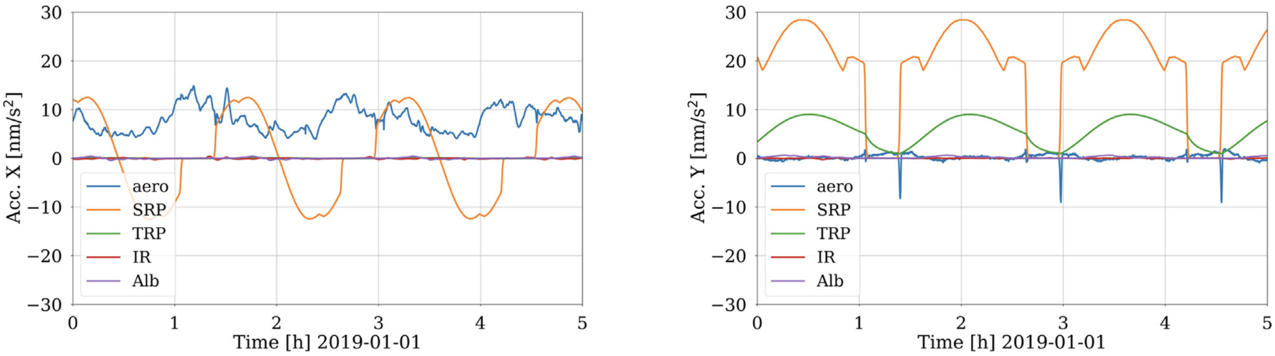

Fig. 5. Non-gravitational forces acting on the GRACE-C satellite: aerodynamic acceleration (aero), Solar Radiation Pressure (SRP), Thermal Radiation Pressure (TRP), Earth's Infrared radiation (IR), Earth's Albedo (Alb).

where P_{ext} stands for the radiation pressure originating from external sources such as solar radiation, Earth's infrared radiation and Earth's albedo, $\boldsymbol{C}_w$ is the coefficient integrated over the relevant wavelength domain, and m is the satellite mass. The α and β angles describe the satellite orientation toward the incident radiation. They can be derived using a unit vector fixed to the satellite reference frame, $\boldsymbol{u}_{sat}$, pointing from the radiation source towards the satellite:

$$\boldsymbol{u}_{\mathrm{sat}} = \begin{bmatrix} u_x \\ u_y \\ u_z \end{bmatrix}, \quad \alpha = \arcsin(u_z), \quad \beta = \arctan_2(u_y, -u_z). \tag{5}$$

The main contributor to the radiation pressure is solar radiation pressure, commonly defined as

$$P_{\mathrm{srp}} = \left(\frac{1\mathrm{AU}}{\|\boldsymbol{r}_{sat} - \boldsymbol{r}_{Sun}\|}\right)^2 P_{1\mathrm{AU}}, \tag{6}$$

where $\boldsymbol{r}_{sat}$ and $\boldsymbol{r}_{Sun}$ are the positions of the satellite and Sun, respectively. $P_{1\mathrm{AU}}$ is the solar radiation pressure at one astronomical unit (AU), commonly calculated as the ratio of the solar constant $\Phi = 1367\mathrm{Wm}^{-2}$ and the speed of light c, i.e. $P_{1\mathrm{AU}} = \Phi/c = 4.56\mu\mathrm{Nm}^{-2}$. The calculation of radiation forces originating from Earth's albedo and infrared radiation is described by Vielberg and Kusche (2020), noting that we use monthly averaged albedo and Earth infrared emission maps based on Earth Radiation Budget Experiment (ERBE) satellite data (Doornbos et al., 2014).

This study employs a ray-tracing technique to calculate the radiation pressure coefficient $\boldsymbol{C}_w$. This technique uses the high-fidelity GRACE-FO geometry as input, previously described in Section 2.3. Ray-tracing simulates the scenario in which a distant radiation source emits parallel rays towards a much smaller satellite body. The algorithm accounts for both self-shadowing and multiple reflections. Emitted rays intersect with the satellite surface and spawn additional rays, whose energy depends on the surface properties. We use the ray tracing technique to calculate the solar radiation pressure, Earth's infrared radiation, and albedo (Siemes et al., 2023).

3.2. Thermal emission modelling

The thermal model proposed in this article is similar to the approach suggested and implemented by Wöske et al. (2019). We modelled the satellites by 12 independent panels and the inner body. The panels heat up uniformly by absorbing incoming radiation $\dot{Q}_{\mathrm{abs},j}$, cool down by emitting radiation $\dot{Q}_{\mathrm{emit},j}$ and exchange heat $\dot{Q}_{\mathrm{cond},j}$ conductively with the satellite body, resulting in the net heat change

$$\dot{Q}_j = (1 - e_j)\,\dot{Q}_{\mathrm{abs},j} - \dot{Q}_{\mathrm{emit},j} - \dot{Q}_{\mathrm{cond},j}, \tag{7}$$

where e_j stands for the electric efficiency, and subscript j indicates the panel. The electric efficiency represents the fraction of absorbed energy converted into electricity. Therefore, $e_j > 0$ for the solar arrays while $e_j = 0$ for the other panels not covered by photovoltaic cells. Introducing the efficiency parameter into the thermal model has been done by multiple authors (Duan and Hugentobler (2022), Wang et al. (2023)). However, it was not the case in formerly published GRACE-FO datasets (Siemes et al., 2023).

The radiation Φ that originates from solar and Earth fluxes, as well as albedo, is absorbed in both visible and infrared bandwidths following the equation

$$\dot{Q}_{\mathrm{abs},j} = \Phi c_{\mathrm{a},j} A_j \cos\theta_j, \tag{8}$$

where $c_{\mathrm{a},j}$ is the absorption coefficient, A_j is the area of the panel, and θ is the angle between the panel's normal and the vector from the satellite to the radiation source. The heat loss toward space follows the Stefan–Boltzmann law of diffuse irradiation:

$$\dot{Q}_{\mathrm{emit},j} = A_j \varepsilon_j \sigma T_j^4, \tag{9}$$

where ε_j is the emissivity, σ is the Stefan–Boltzmann constant and T_j is the absolute temperature of the satellite panels.

The thermal conduction between the satellite walls and the inner body T_{body} is

$$\dot{Q}_{\mathrm{cond},j} = k_j(T_j - T_{\mathrm{body}}), \tag{10}$$

where k_j is the thermal conductivity. The total heat exchange for the satellite body is

$$\dot{Q}_{\mathrm{body}} = \dot{Q}_{\mathrm{gen}} + \sum_j \dot{Q}_{\mathrm{cond},j}, \tag{11}$$

where $\dot{Q}_{\mathrm{gen}}$ stands for the internal heat generated by, e.g., the batteries and electronics. The $\dot{Q}_{\mathrm{gen}}$ value was selected to assure the realistic operational inner temperature T_{body} of about 25°C.

In the numerical implementation, panels and body temperatures are updated at each timestep following the equations

$$T_j(t + \Delta t) = T_j(t) + \frac{\dot{Q}_j}{C_j}\Delta t, \tag{12}$$

and

$$T_{\mathrm{body}}(t + \Delta t) = T_{\mathrm{body}}(t) + \frac{\dot{Q}_{\mathrm{body}}}{C_{\mathrm{body}}}\Delta t, \tag{13}$$

where C_j and C_{body} are the thermal capacity of the panels and the satellite body, respectively.

Finally, the thermal radiation pressure acceleration is derived using the following formula

$$\boldsymbol{a}_{\mathrm{the}} = -\frac{2}{3}\sum_j \frac{\dot{Q}_{\mathrm{emit},j}}{mc}\boldsymbol{n}_j, \tag{14}$$

where $\boldsymbol{n}_j$ is the outer panel normal of the j surface element.

The following control parameters describe the thermal model: heat capacity of the panels, thermal conductance towards the inner parts, solar cell efficiency, and internal heat generated by the payload and other electronic parts. We optimise the control parameters by minimising the Root Mean Square (RMS) of the difference in the y-component of the accelerations $a_{\mathrm{the,y}}$ as calculated in Eq. (14) and $\hat{a}_{\mathrm{the,y}}$ derived directly from the thermistor measurements:

$$RMS = \sqrt{\frac{\sum_{n=1}^{n}(\hat{a}_{\mathrm{the,y}} - a_{\mathrm{the,y}})^2}{n}}, \tag{15}$$

where n is the number of data points in 2020. We selected this year because of the satellite's high altitude and low solar activity.

3.3. Surface coefficients fine-tuning

As previously explained in Section 3.1, the radiation pressure coefficients were derived using the ray-tracing algorithm. We introduce the sum of the contributions of the individual materials m:

$$\boldsymbol{a}_{\mathrm{rp}}(\alpha,\beta) = \frac{P_{\mathrm{ext}}(\alpha,\beta)}{m}\sum_m(\boldsymbol{C}_{\mathrm{a,m}}c_{\mathrm{a,m}} + \boldsymbol{C}_{\mathrm{d,m}}c_{\mathrm{d,m}} + \boldsymbol{C}_{\mathrm{s,m}}c_{\mathrm{s,m}}). \tag{16}$$

The factors $c_{\mathrm{a,m}}, c_{\mathrm{d,m}}$, and $c_{\mathrm{s,m}}$ denote coefficients of absorption, diffuse and specular reflections, respectively, while $\boldsymbol{C}_{\mathrm{a,m}}, \boldsymbol{C}_{\mathrm{d,m}}$, and $\boldsymbol{C}_{\mathrm{s,m}}$ are radiation pressure coefficient vectors. These vectors originating from the intersection of the i-th ray, with the j-th surface element, and then summing all intersections with surface elements of the same material (sum over index i), are defined as

$$\boldsymbol{C}_{\mathrm{a,m}} = \sum_i A_i \boldsymbol{r}_i \tag{17}$$

for absorption,

$$\boldsymbol{C}_{\mathrm{d,m}} = \sum_i A_i(r_i - \frac{2}{3}\boldsymbol{n}_j) \tag{18}$$

for diffuse reflection, and

$$\boldsymbol{C}_{\mathrm{s,m}} = \sum_i 2A_i(r_i \cdot \boldsymbol{n}_j)\cdot \boldsymbol{n}_j \tag{19}$$

for specular reflection. Calculating the sum of all surface elements with the same material allows us to extract the individual materials' contribution to the total radiation pressure. This equation holds for both infrared and visible light. However, this analysis focuses only on the latter. It is because the magnitude of the Earth's infrared radiation is much smaller than the solar radiation in the along-track and cross-track directions (Vielberg and Kusche, 2020), which are relevant for the density and crosswind observations. In the selected period for GRACE-C, the infrared radiation pressure acceleration was smaller than 0.5 nms^{-2} in both x and y directions. In comparison, the size of the SRP acceleration was about 12 nms^{-2} in the along-track and about 28 nms^{-2} in the cross-track direction, respectively.

To realistically represent GRACE-FO characteristics, a new set of finetuned coefficients c_m, describing surface properties is necessary. In the first step, the density based on the along-track acceleration (Eq. (3)) was used to derive the acceleration in the y-direction due to aerodynamic side forces,

$$a_{\mathrm{aero},y,der} = \frac{C_{\mathrm{aero},y}}{C_{\mathrm{aero},x}}a_{\mathrm{aero},x}, \tag{20}$$

where $C_{\mathrm{aero,y}}$ is the aerodynamic coefficient vector, multiplied by the corresponding cross-section area, and $a_{\mathrm{aero},y,der}$ stands for the y-component of aerodynamic acceleration derived from the along-track signal.

Afterwards, we calculated the difference

$$\Delta a_{\mathrm{aero},y} = a_{\mathrm{aero},y} - a_{\mathrm{aero},y,der}, \tag{21}$$

between the derived cross-track acceleration and the observed one. We selected a time period of one year (2020) to optimise the radiation pressure model. This selection is motivated by the high GRACE-FO altitude of approximately 510 km, the very low solar activity during that period, and the fact that all local solar times are covered within one year. Under such conditions, the acceleration due to crosswind is negligible, and $\Delta a_{\mathrm{aero},y}$ should thus equal zero. Since the aerodynamic acceleration depends on the radiation pressure acceleration $\boldsymbol{a}_{\mathrm{rp}}$ and thermal acceleration $\boldsymbol{a}_{the}$ (cf. Eq. (1) and Eq. (2)), we used it directly to determine new coefficients. We note that $\boldsymbol{a}_{the}$ was calculated from the thermistor measurements as described in Section 3.2.

In the next step, a highpass filter was applied to $\Delta a_{\mathrm{aero},y}$ to eliminate the influence of the accelerometer data calibration, which affects daily and longer periods (Siemes et al., 2023):

$$\Delta a_{\mathrm{aero},y,filt} = \mathrm{filt}\left(\Delta a_{\mathrm{aero},y}\right). \tag{22}$$

In contrast to the accelerometer data calibration, radiation pressure modelling errors also affect the sub-daily variations in $\Delta a_{\mathrm{aero},y}$, e.g., step-like changes at the eclipse entry and exit locations. Applying a highpass filter allows us to focus on these errors and, therefore, optimise the reflection coefficients without any impact from the accelerometer data calibration.

The radiation pressure acceleration can be defined as a function of the absorption and reflection coefficients per material:

$$f(c_{a,m}, c_{d,m}, c_{s,m}) = \| \Delta a_{\mathrm{aero},y,filt} \|. \tag{23}$$

Finally, we use the Sequential Least SQuares Programming (SLSQP) technique originally implemented by Kraft (1988) to minimise $f(c_{a,m}, c_{d,m}, c_{s,m})$. The SLSQP algorithm allows minimising a linear function of several variables subject to bounds and constraints, here defined as:

$$\begin{aligned} &c_{\mathrm{a,m}} \in [0,1], \quad c_{\mathrm{d,m}} \in [0,1], \\ &c_{\mathrm{s,m}} \in [0,1], \qquad c_{\mathrm{a,m}} + c_{\mathrm{d,m}} + c_{\mathrm{s,m}} = 1. \end{aligned} \tag{24}$$

The optimum solution was computed after 15 iterations. The fine-tuned surface coefficients are provided in Table 2 (Section 4.2).

Apart from optimising the surface properties, $\Delta a_{\mathrm{aero},y}$ as defined in Eq. (21) serves to calibrate the cross-track acceleration. When the calibration is only based on precise orbit determination (POD), the cross-track calibration accuracy suffers from, e.g., dynamic force model errors, which renders the crosswind observations unusable. To resolve this, we first optimise the radiation pressure modelling to mitigate errors from this source as much as possible. Then, we recalculate $\Delta a_{\mathrm{aero},y}$ and apply a lowpass filter that removes sub-daily variations to extract the accelerometer data calibration and remaining radiation pressure modelling errors (Siemes et al., 2023). The lowpass filtered $\Delta a_{\mathrm{aero},y}$ is directly applied as a correction to the cross-track accelerations.

4. Results and discussion

4.1. Thermal emission modelling

The design of solar arrays of GRACE and GRACE-FO differs. While the GRACE satellites were equipped with silicon cells, its successors utilize modern triple-junction gallium arsenide (GaAs) cells with an efficiency of 28% (Kornfeld et al., 2019). Since the proposed thermal model is based on the panel model, we must distinguish between the area covered by photovoltaic cells and the panel area, partly covered by multi-layer insulation (MLI) foil, star trackers, and other elements. Based on the technical drawings (Fig. 2) the exact number of solar cells n was estimated for solar arrays $n_{SA} = 656$ and the zenith panel $n_{zenith} = 479$. The area of the individual cell is known to be A_{cell}=31.36 cm. Using this information, the packing factor p can be calculated as a ratio between the effective area covered by the solar cells, and the total panel area

$$p = \frac{A_{cell} * n}{A_{total}}. \tag{25}$$

Following this equation the packing factor was estimated to be 0.66 for the side panels and 0.69 for the zenith panel, resulting in the panel efficiency of 18% and 19%, respectively.

The design difference between GRACE and GRACE-FO solar arrays also affects the visible and infrared surface coefficients as they control how much energy is absorbed or reemitted. Table 2 provides optimised coefficients for visible light. The emissivity was specified according to the Swarm technical note on thermo-optical properties (Siemes, 2019), noting that the Swarm solar array is the same as on GRACE-FO. In the proposed modelling approach the emissivity, as well as efficiency, fulfil the same function of controlling how much radiation is reemitted. This means that both parameters have almost the same effect on the cross-track acceleration, and therefore cannot disentangle. For this reason, we only modify the efficiency.

We used the in situ thermistor measurements to select the remaining thermal model control parameters, the heat capacity and conductivity. As described in Section 2.2, only external thermistors located on the solar arrays on the side panels and the zenith panel were suitable for such analysis. Since the thermal emission contributes mainly to the cross-track acceleration, the thermistor's locations perfectly align with our modelling requirements.

The first step in optimising the heat capacity and conductivity was to convert thermistors measurements and modelled temperatures into the accelerations following Eq. (14). Since each solar array on the side panels has two temperature sensors, we determined the acceleration difference between both sensor pairs. Fig. 6 shows that the differences do not surpass 0.6 nms^{-2}, which was used as a reference for the maximum reachable modelling accuracy, noting that our model assumes a uniform temperature per panel.

In the second step, we compared the accelerations based on the measured temperatures, $\hat{a}_{the,y}$, and the modelled temperatures, $a_{the,y}$, for a range of capacity and conductivity values using the RMS defined in Eq. (15). Fig. 7 and Fig. 8 summarise the results. For the solar arrays, the best fit (RMS $= 0.148\mathrm{nm}\ \mathrm{s}^{-2}$) was obtained for heat capacity

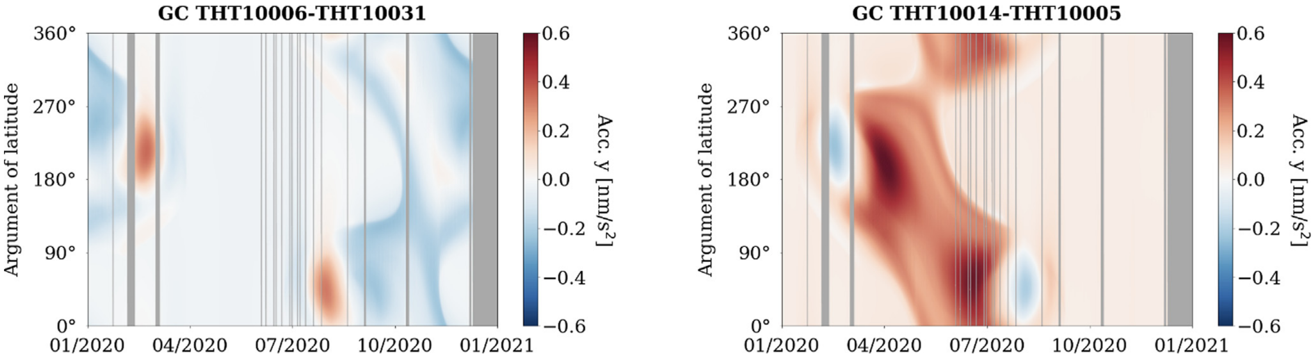
GC THT10006-THT10031

GC THT10014-THT10005

Fig. 6. Comparison between the measurements of thermistors located on the same solar array, translated into acceleration.

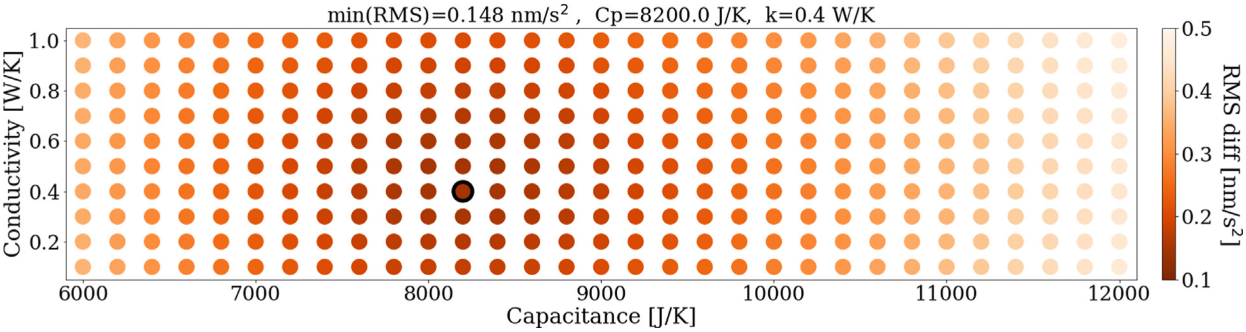

Fig. 7. Root Mean Square (RMS) acceleration difference between the thermal model and the THT10005/THT10031 thermistors. The best fit was obtained for capacity $C = 8200.0\mathrm{JK}^{-1}$ and conductivity $k = 0.4\mathrm{WK}^{-1}$ The best RMS fit is indicated with the dark circle.

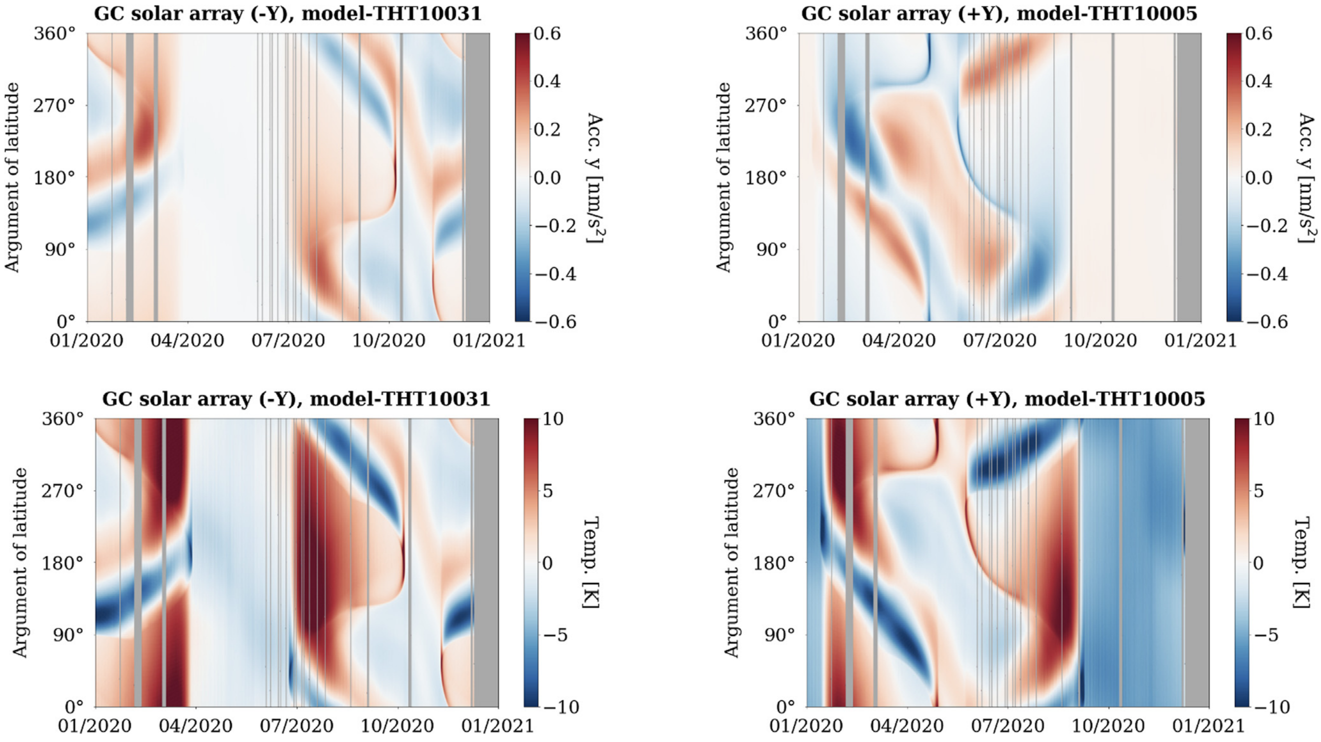
GC solar array (-Y), model-THT10031

GC solar array (+Y), model-THT10005

GC solar array (-Y), model-THT10031

GC solar array (+Y), model-THT10005

Fig. 8. Differences between the accelerations (top) and the temperatures (bottom), derived from the thermal model and measured by thermistors.

$C = 8200.0\mathrm{JK}^{-1}$ and conductivity $k = 0.4\mathrm{WK}^{-1}$. Such parameter selection assures that the thermal model accuracy is within the earlier defined range of 0.6 nms^{-2} (Fig. 6).

We performed a similar analysis for the zenith panel, for which external temperature sensors are also available. The best fit was found for $C = 5800.0\mathrm{JK}^{-1}$ and $k = 0.7\mathrm{WK}^{-1}$. The difference between solar arrays and zenith thermal parameters is likely caused by different packing factors of the solar cells.

This analysis focused on optimising the thermal model for the panels for which the thermistor measurements were available. The remaining values of heat capacities and conductivities were defined according to the GRACE-FO thermal model developed by Siemes et al. (2023). Table 1 summarises the updated parameters and previously used values.

4.2. Surface coefficients fine-tuning

This section reports the results of the surface coefficient optimization using the method described in Section 3.3 and summarized in Table 2. The first column describes the material, whereas the next column provides initial values of the optical coefficients from the GRACE-FO Level-1 Data Product User Handbook (Ying et al., 2019) and recently redefined values from Siemes et al. (2023). The last columns consist of the coefficients optimized within this study. The coefficients for infrared radiation are defined in the handbook and were not modified. These coefficients have an insignificant effect on the y-acceleration and could not be finetuned with the method presented in this paper.

In addition to the SLSQP fitting of the coefficients, we inspected the satellite photos visually to cross-check updated thermo-optical surface coefficients. One of the fundamental design differences between GRACE-FO (Fig. 1) and its predecessor was replacing the silicon solar cells (Si Glass) with state-of-the-art triple-junction gallium arsenide (GaAs) cells, previously certified for the Swarm mission (Kornfeld et al., 2019). These solar arrays absorb more light and, thus, have a higher efficiency. This design similarity between Swarm and GRACE-FO justifies the selection of optical absorption (c_a=0.90), which coincides with the value provided in Swarm technical note on thermo-optical properties (Siemes, 2019).

The second dissimilarity visible in the prelaunch photos (Fig. 1) is the difference in the solar arrays' packing factor of the side panels and the zenith panel. The zenith panel is more densely populated by the solar cells (black) compared to the two side panels, which reveal more of the background MLI foil (red). Since the ray-tracing algorithm treats the MLI and solar cells (depicted as red and black surface elements) uniformly, the packing factor affects the overall absorptivity of this material (c_s=0.90 → c_s=0.88).

Another distinctive element between GRACE and GRACE-FO is the nadir panel (red circles in Figs. 9a

Table 1
GRACE-FO thermal radiation panel model. The internal heat generation was set to 55 W, and the satellite body heat capacity to $1 \times 10^5\mathrm{JK}^{-1}$.

Panel	A_j (m^2)	$n_{x,j}$ (-)	$n_{y,j}$ (-)	$n_{z,j}$ (-)	Siemes et al. (2023) C_j (JK^{-1})	Siemes et al. (2023) k_j (WK^{-1})	New thermal model C_j (JK^{-1})	New thermal model k_j (WK^{-1})	New thermal model e_j (-)
Front	0.9551567	1.0	0.0	0.0	4000.0	0.1	4000.0	0.1	-
Rear	0.9551567	−1.0	0.0	0.0	4000.0	0.1	4000.0	0.1	-
Starboard (outer)	3.1554792	0.0	0.766044	−0.642787	18000.0	0.1	8200.0	0.4	0.18
Starboard (inner)	0.2282913	0.0	−0.766044	0.642787	800.0	0.1	800.0	0.1	-
Port (outer)	3.1554792	0.0	−0.766044	−0.642787	18000.0	0.1	8200.0	0.4	0.18
Port (inner)	0.2282913	0.0	0.766044	0.642787	800.0	0.1	800.0	0.1	-
Nadir	6.0711120	0.0	0.0	1.0	10000.0	0.5	10000.0	0.5	-
Zenith	2.1673620	0.0	0.0	−1.0	12000.0	0.1	5800.0	0.7	0.19
Boom*	0.0461901	-	-	-	400.0	0.01	400.0	0.01	-

* Planar projection area of the cylindrical Boom, along X-Y plane.

Table 2
Comparison between GRACE-FO surface coefficients for visible light: defined in Level-1 Data Product User Handbook (Ying et al., 2019) (1), provided by Siemes et al. (2023) (2), and fine-tuned within this study (3). Surface coefficients for infrared radiation are defined in Level-1 Data Product User Handbook.

(1) Material	(1) Level-1 Handbook c_a	(1) Level-1 Handbook c_d	(1) Level-1 Handbook c_s	(2) Siemes et al. (2023) c_a	(2) Siemes et al. (2023) c_d	(2) Siemes et al. (2023) c_s	(3) Fine-tuned coefficients c_a	(3) Fine-tuned coefficients c_d	(3) Fine-tuned coefficients c_s
SiOx/Kapton (Front/Rear)	0.34	0.26	0.40	0.34	0.26	0.40	0.14	0.15	0.71
SiOx/Kapton (Apron)	0.34	0.26	0.40	0.34	0.26	0.40	0.05	0.79	0.16
Si Glass (Solar Arrays)	0.65	0.30	0.05	0.90	0.07	0.03	0.90	0.10	0.00
Si Glass (Zenith)	0.65	0.30	0.05	0.90	0.07	0.03	0.88	0.00	0.12
Teflon (Nadir)	0.12	0.20	0.68	0.12	0.20	0.68	0.00	0.05	0.95

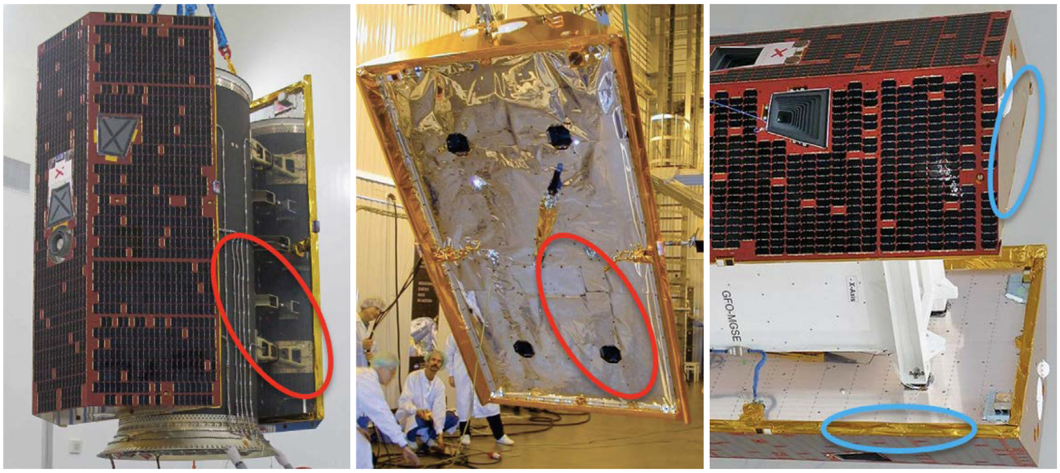

(a) GRACE-FO[4] (b) GRACE[5] (c) GRACE-FO[6]

Fig. 9. Prelaunch photos of GRACE-FO[4, 6] and GRACE[5] satellites. Red circles (a) and (b) show the differences in the nadir panel design between two satellites. Blue circles (c) indicate the differences in the material of the apron and the rear panel.

Table 3
The summary of GRACE-FO radiation pressure modelling approaches implemented in this study.

Case	Thermal model –	Geometry model –	Surface properties –	RMS (nms^{-2})
(a)	-	Panel	Level-1 Handbook	4.22
(b)	Instantaneous reradiation	Panel	Level-1 Handbook	3.04
(c)	Thermal inertia	Panel	Level-1 Handbook	1.70
(d)	Thermal inertia	Ray-tracing	Siemes et al. (2023)	0.88
(e)	Thermal inertia	Ray-tracing	Fine-tuned coefficients	0.55

and 9b). The GRACE nadir panel has a much more creased surface than the reflective GRACE-FO material. This difference justifies finetuning the specular reflection coefficient to the higher value (c_s=0.68 → c_s=0.95).

Ultimately, we finetuned the satellite's apron surface coefficients. This small geometry element proved to have a significant impact on the radiation pressure acceleration. The Handbook defines the surface properties of the apron and the rear/front panels as identical. However, the photos reveal that the front/rear panels have a reflective surface, whereas the apron is creased and, thus, reflects light more diffusely than a flat surface of the same material (Fig. 9c). Such difference validates the increase in the diffuse reflection component (c_d=0.26 → c_d=0.79).

4.3. Effect of radiation pressure model accuracy on the cross-track acceleration

As discussed before, the cross-track calibration purely based on POD suffers from low accuracy, affecting the quality of crosswind data. The exact steps undertaken to resolve this issue were described in Section 3. Here, we used the $\Delta a_{aero,y}$ parameter derived in Eq. (21) to assess the performance of various radiation pressure and thermal emission modelling approaches. The calibration parameters were estimated based on the final model (Case (e), Table 3) and applied consistently to all previous cases. This approach enabled disentangling the calibration parameters' accuracy and focus on the sole impact of the radiation pressure modelling.

Table 3 summarises models used in this study, together with their input parameters: thermal emission model, geometry model and the thermo-optical surface coefficients used. The last column states the RMS estimate as the model quality indicator.

The most straightforward approach to radiation pressure modelling is presented in Fig. 10a. It utilizes the simplest geometry consisting of 6 panels and does not account for thermal emission. The thermo-optical surface properties used for the radiation pressure modelling follow the guidelines provided in the Level-1 Handbook. In this modelling variant, the acceleration difference $\Delta a_{aero,y}$ exceeds the RMS of 4.22 nms^{-2}. The largest offset occurs when the satellite solar arrays on the sides of the satellite (red area in Fig. 4) are oriented perpendicular to the Sun. These

---

[4] airbus.com/en/newsroom/press-releases/2017-05-grace-fo-satellites-get-an-earful accessed on 03/10/2023.

[5] Gath (2016)

[6] www.airbus.com/en/newsroom/press-releases/2017-05-grace-fo-satellites-get-an-earful accessed on 03/10/2023.

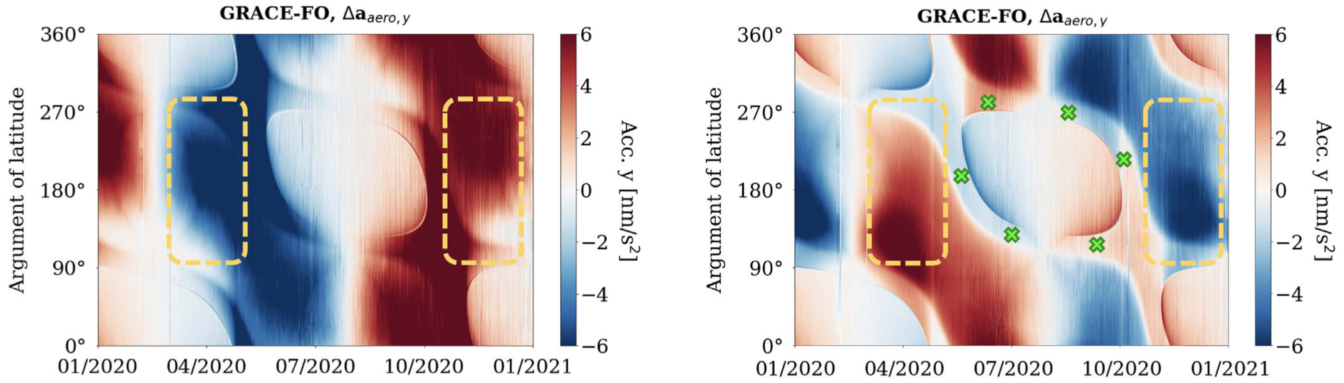

(a) Not accounting for the thermal emission acceleration.

(b) Instantaneous thermal reradiation.

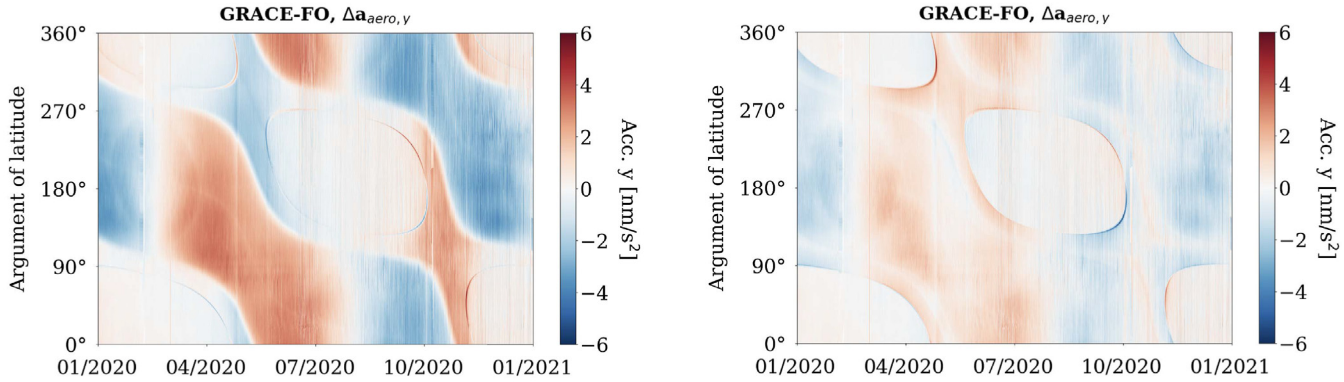

(c) Thermal inertia and panel method.

(d) Thermal inertia and ray-tracing method.

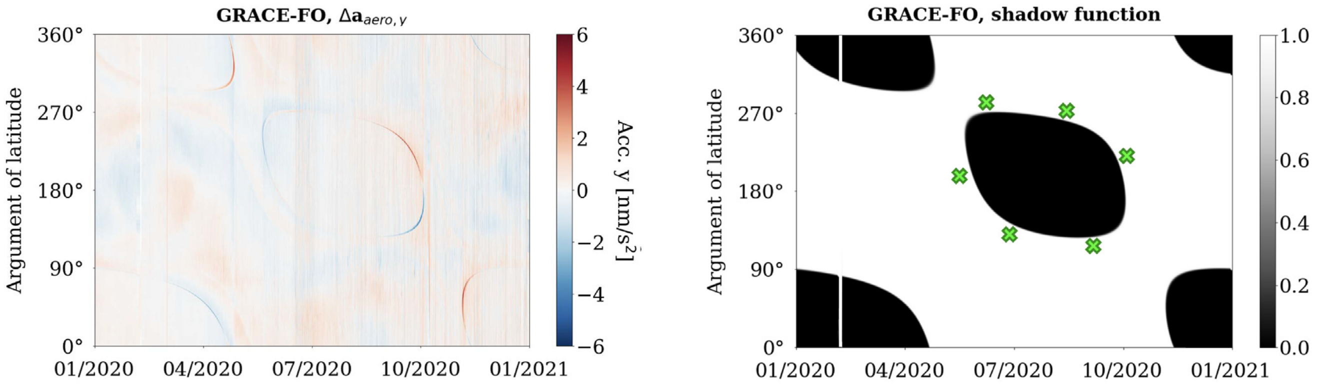

(e) Thermal inertia and fine-tuned thermo-optical surface properties.

(f) Shadow function.

Fig. 10. Difference between observed and derived cross-track acceleration $\Delta a_{\mathrm{aero},y}$ defined in Eq. (20) for cases (a)–(e) (cf. Table 3) and the shadow function. White and black areas indicate when the satellite is in the sunlight or shadow. The yellow dashed-line rectangles indicate when the satellite solar arrays were oriented perpendicular to the Sun. The green crosses mark locations when the satellite is close to the penumbra regions. (For interpretation of the references to colour in this figure legend, the reader is referred to the web version of this article.)

locations are indicated by yellow dashed rectangles (Fig. 10a). At this stage, the cross-track acceleration errors originate mainly from ignoring the thermal emission of the solar arrays, as demonstrated in the next paragraphs.

The second model, illustrated in Fig. 10b, assumes instantaneous heat reradiation for all panels (Montenbruck et al., 2015), i.e. the absorbed radiation is instantly re-emitted in accordance with Lambert's cosine law. The main difference in comparison to Case (a) can be noted in the radiation pressure errors originating from the solar arrays. It occurs when the solar arrays are oriented approximately perpendicular to the Sun, which takes place between the arguments of latitude 90° and 270°, during April 2020 for the (+Y) solar array and November 2020 for (-Y) solar array. Similar to the previous figure, these locations are indicated by yellow dashed rectangles. The second effect can be spotted near the eclipse regions, which can be identified based on the shadow function shown in Fig. 10f, indicated as green crosses. This effect occurs when the satellite enters the eclipse, and the nadir panel receives direct radiation, which is then re-radiated. Since this scenario better reflects reality, the radiation pressure errors decrease compared to Case (a). Using the instantaneous heat re-radiation model, the overall radiation pressure error $\Delta a_{\mathrm{aero},y}$ reduces to RMS 3.04 nms^{-2}.

Fig. 10c was produced using a thermal model that accounts for the thermal inertia of the panels as described in Section 3.2. The optimized thermal control parameters are provided in Table 1. In this variant, the panel geometry was used for both radiation pressure and thermal emission modelling. After accounting for the thermal inertia the $\Delta a_{\mathrm{aero},y}$ decreases significantly, to RMS 1.70 nms^{-2}.

In the next step, we complemented the advanced thermal modelling with ray-tracing utilizing the high-fidelity geometry and the thermo-optical surface coefficients proposed by Siemes et al. (2023), provided in Table 2. The model's output is depicted in Fig. 10d. Including additional geometry elements creates a more uniform error pattern. An interesting effect, exhibiting as $\Delta a_{\mathrm{aero},y}$ reduction around the eclipse transitions, was identified as a shadowing effect from the satellite's apron. In this step, the cross-track acceleration RMS is reduced to 0.88 nms^{-2}.

Last but not least, Fig. 10e shows the thermal emission modelling improvements combined with the ray-tracing method, detailed satellite geometry, and fine-tuned thermo-optical surface coefficients (Table 2). Introducing these improvements altogether results in the significant reduction of the $\Delta a_{\mathrm{aero},y}$ errors below 0.55 nms^{-2}.

The remaining radiation pressure residuals could be caused by errors in the thermistors' measurements, as well as the modelling limitations, e.g., the assumption of the uniform temperature of the panels. To resolve this issue, we could introduce a finite element thermal model. However, such a modelling approach is computationally demanding and unlikely to give significant improvement due to other error sources, which are out of the scope of this work. These error sources include the assumption about negligible cross-wind during low solar activity while fine-tuning the surface coefficients, aerodynamic coefficient modelling errors originating from the gas-surface interaction modelling uncertainties, and accelerometer data calibration errors. To model the penumbra transitions, this paper utilizes the Solar radiation pressure with Oblateness and Lower Atmospheric Absorption, Refraction, and Scattering Curve Fit (SOLAARS-CF) (Robertson et al., 2015). However, using this approach results in noticeable artefacts remaining around the eclipse entrances/exits. Therefore, these times were excluded while calculating the RMS.

4.4. Density and crosswind observations

The new GRACE-FO density and crosswind datasets, labelled V2b, are available from the FTP server ftp://thermosphere.tudelft.nl. Compared to the previous version V2 in Siemes et al. (2023), this new version contains two major improvements. Firstly, it is based on the fine-tuned surface coefficients for the radiation pressure modelling. Secondly, it introduces the electrical efficiency of the solar arrays into the thermal model and optimises its parameters based on real temperature data.

4.4.1. Crosswind

To analyse the impact of the radiation pressure modelling on the crosswind data, we selected a time period of increasing solar activity from 2022 until mid-2023. Fig. 11 shows the 3-hourly geomagnetic activity index ap and 10.7 cm solar radio flux ($F_{10.7}$). Fig. 12 compares the log RMS ratio of the radiation pressure acceleration to the aerodynamic acceleration for GRACE-C with a sliding window of one week. For the selected period, the magnitude of the aerodynamic acceleration surpasses the magnitude of radiation pressure in the along-track direction. For the cross-track direction, the RMS ratio reflects the trend of the $F_{10.7}$ curve (Fig. 11). At the beginning of 2022, the magnitude of the radiation pressure acceleration is 10 times larger in comparison to the aerodynamic acceleration. Fig. 12 shows that this difference gradually decreases with increasing solar activity in 2023. The low periodic RMS ratio values for cross-track acceleration occur when the Sun is aligned with the orbital plane, resulting in accelerations from the right and left solar array cancelling out.

Fig. 13 compares versions V2 and V2b of the observed GRACE-C crosswind. The argument of latitude used in the figures in this section is described in Section 2.2. Qualitatively, both versions have several similarities. The wind speeds peak near the poles (close to arguments of latitude 90° and 270°), which is associated with the auroral oval (Lühr et al., 2007), and are generally less than 150m s^{-1} in the low- and mid-latitudes. Around the north pole (90°±20°), 4% of wind speed exceeds 500m s^{-1}, whereas 9% is larger than 400m s^{-1}. Around the south pole (270°±20°) the wind speed is slightly lower, with only 2% exceeding 500m s^{-1}, and 5% being larger than 400m s^{-1}. Magnetospheric convection and particle precipitation contribute to energy and momentum transfer between ions, drifting rapidly in electric and magnetic fields, and neutrals, which strongly influence the high-latitude thermosphere, including neutral winds (e.g., Barreto-Schuler et al., 2021; Killeen and Roble, 1984; Richmond et al., 2003).

The sharp curve features present in both V2 and V2b in Fig. 13 are an artefact due to eclipse transitions caused by inaccurate modelling of the Earth's shadow. The high wind speeds around January and August/September 2022 visible in both versions in Fig. 13 also correspond to periods of low signal-to-noise in the measured along track acceleration. Under such conditions, meaningful wind retrieval is limited. This results in spurious features that cannot be mitigated by improvements in radiation pressure modelling alone. In order to distinguish the useful wind data from the spurious features, we have introduced flagging in the published dataset.

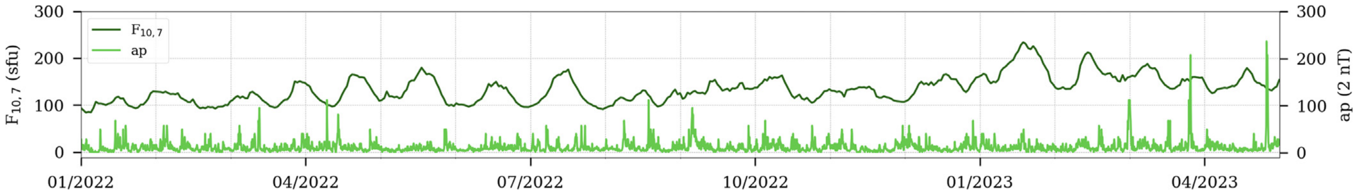

Fig. 11. 3-h ap (source: GFZ German Research Center for Geosciences) and 10.7 cm solar radio flux ($F_{10.7}$). $1\,\mathrm{sfu} = 10^{-22}\cdot\mathrm{W}\cdot\mathrm{m}^{-2}\cdot\mathrm{Hz}^{-1}$.

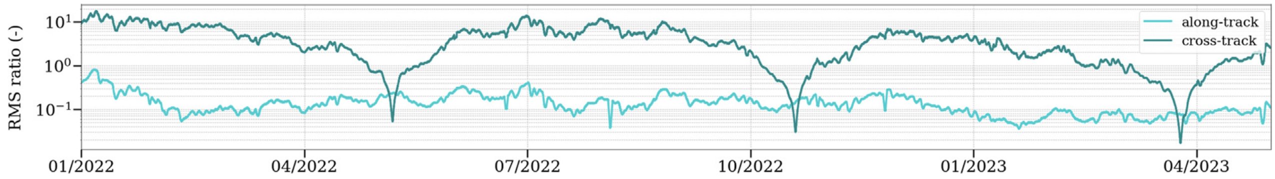

Fig. 12. Size of the radiation pressure acceleration relative to the aerodynamic acceleration for GRACE-C, where the size is measured by the RMS of the acceleration within a sliding one-week window.

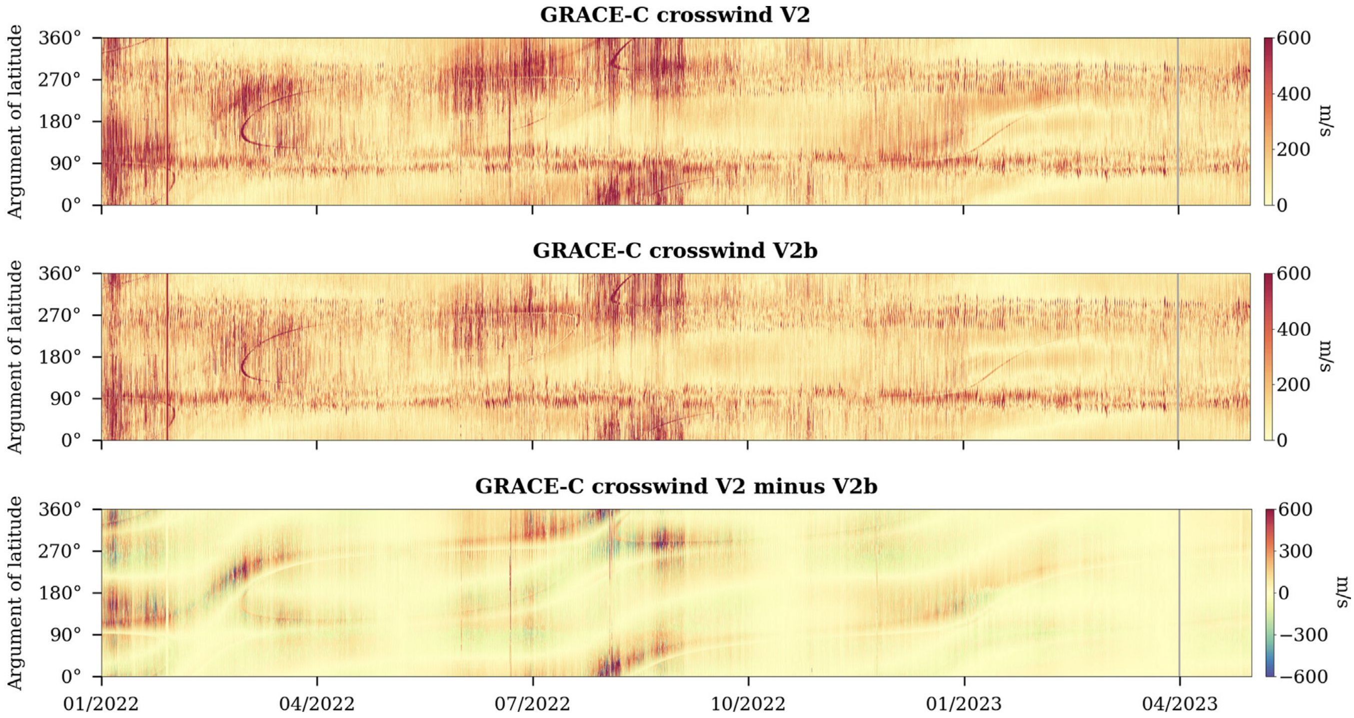

Fig. 13. GRACE-C crosswind speed version V2 (top, cf. Siemes et al. (2023)), version V2b (middle, this work), and the difference between the two versions (bottom). The values on the x-axis are common for all plots.

The two versions show large differences in 2022, when the ratio of the radiation pressure to aerodynamic acceleration is still significant (see Fig. 12). This demonstrates that the radiation pressure models used to produce V2b are superior to V2. In 2023, as solar activity and hence density increase, the difference between the two versions gradually converges. However, the improvements are still visible in periods such as February/March 2023 during the entry and exit of the eclipse, when the wind speed decreases at mid-latitudes.

In Fig. 14, we compare the new V2b crosswind data with the physics-based TIE-GCM and the empirical HWM14 models. The crosswind data are given in the same reference frame as the models, and the zonal (east–west), meridional (north–south) and vertical unit vector components are provided in the dataset to accurately project the model winds. The contributions from the vertical wind component are much weaker than the horizontal components and are therefore ignored in this study, similar to Lühr et al. (2011) using CHAMP observations. The model wind vector projected onto the direction of the observed crosswind is obtained as follows:

$$\mathbf{M}_{cw,i} = \mathbf{M}_{zonal,i}\cdot\mathbf{u}_{zonal,i} + \mathbf{M}_{merid,i}\cdot\mathbf{u}_{merid,i}, \tag{26}$$

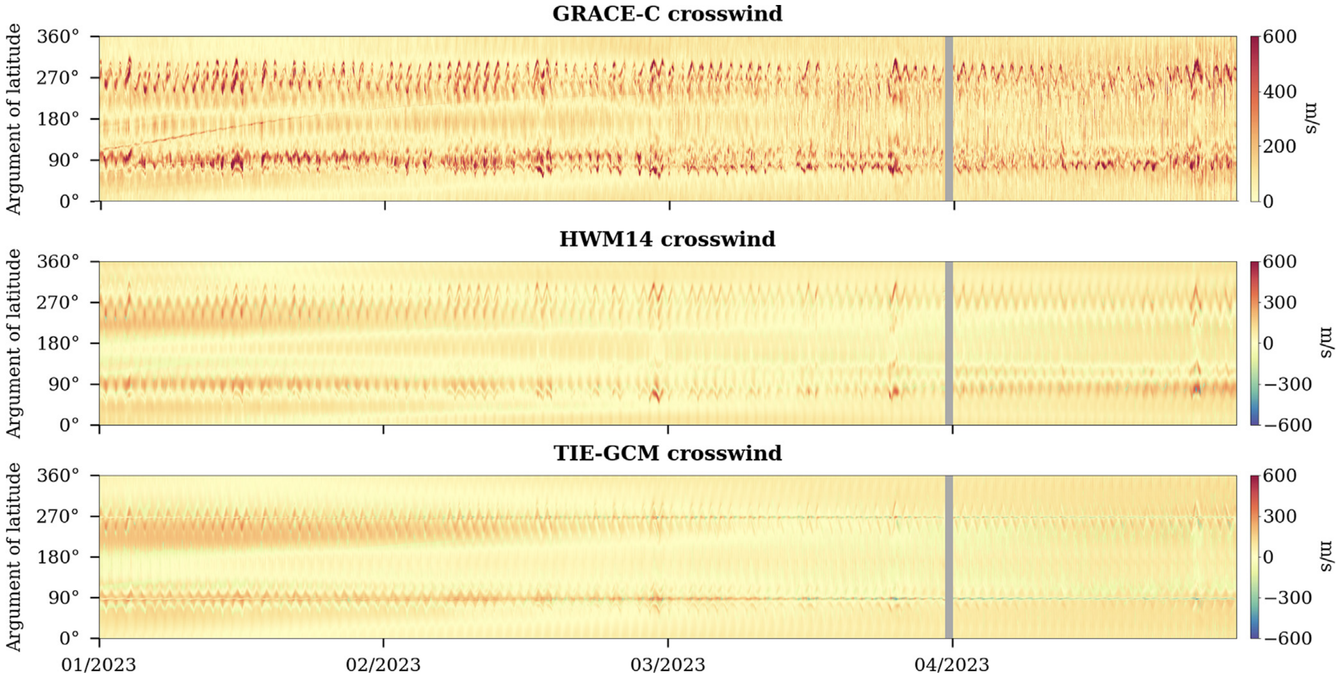

Fig. 14. Crosswind speed observed by the GRACE-C satellite (top), wind speed from the HWM14 model (middle) and TIE-GCM (bottom). The negative values in the model winds indicate that the wind direction is opposite to the observed wind. The values on the x-axis are common for all plots.

where $\mathbf{M}_{cw,i}$ is the projected model crosswind at time epoch i, and $\mathbf{M}_{zonal}$ and $\mathbf{M}_{merid}$ are the model zonal and meridional wind vectors, respectively. $\mathbf{u}_{zonal}$ and $\mathbf{u}_{merid}$ are the corresponding unit vector components.

Fig. 14 shows that both models capture most of the salient features of the observed crosswind, especially at low and mid latitudes. The time period shown in the figure corresponds to relatively high solar activity, which improves the quality of the retrieved wind signal. Compared to the TIE-GCM, the HWM14 shows better agreement at high latitudes and well reflects some of the high wind speed around 90° and 270° occurring during the significant geomagnetic storms in late February, March, and April 2023 (see Fig. 11). In general, the data-model agreement is better in 2023 than in 2022. While the crosswind speeds are greater than the model estimates, this agreement has improved in 2023 to the extent that the mean model wind speed is about half that of the observed crosswind. Further investigation is needed to determine the extent to which the TIE-GCM underestimates the winds, particularly at high latitudes. Neutral winds at high latitudes are strongly influenced by the direction and strength of the interplanetary magnetic field (IMF) and ion collisions (Richmond et al., 2003). The TIE-GCM runs in this study do not use observed IMF conditions and use, among other parameterisations, an empirical ion convection model based on the 3-h Kp index, which may have some limitations in accurately modelling ion drag and winds on the observed timescale.

Fig. 15 shows some general statistics of the data-model comparison from January 2022 to April 2023. The two top panels show the daily mean and standard deviation, respectively. Two bottom panels show the Pearson correlation coefficient, which describes the linear correlation between the models and the observations. Since both TIE-GCM and HWM14 underestimate the high-latitude wind speeds (Fig. 14) the Pearson coefficient was calculated for two subsets: including all data, and considering only low- and mid-latitude crosswinds, by excluding data between arguments of latitude 60°–120° and 240°–300°. The penumbra regions were discarded while calculating the statistical data.

The figure shows a remarkable improvement in the GRACE-C retrieved winds after September 2022, when the daily mean stabilises, the standard deviation is consistently low, and the correlation increases. We observe an exceptionally good correlation after January 2023 reaching 0.6 for all data and 0.8 if only low- and mid-latitude wind speeds are considered. The figure also shows that the GRACE-C crosswinds are quite stable from April to June 2022. There are a few periods in 2022 with large wind speeds and high standard deviations (e.g. January, March and August). As explained earlier, this is due to the spurious features in the crosswind data resulting from an insufficient signal-to-noise ratio in the acceleration data (see Fig. 13). Finally, the figure also highlights the importance of a comprehensive further analysis of the winds to identify the reasons for different model responses to observed geophysical conditions, including the periods of anticorrelated winds in October 2022 and late March 2023.

4.4.2. Density

The newly estimated neutral mass density (V2b) was compared with the previously published data (V2) and two thermosphere models: NRLMSIS 2.0 and DTM2020.

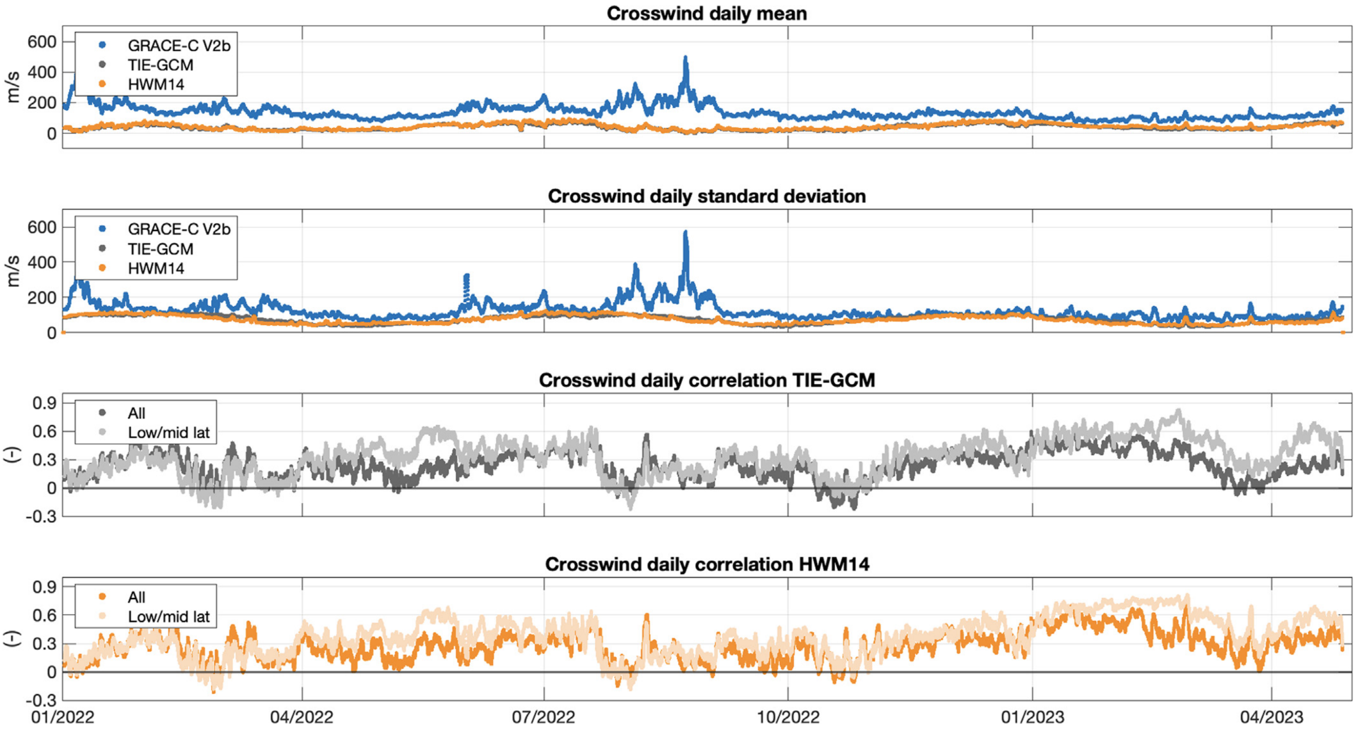

Fig. 15. Statistical comparison of the crosswind speed observed by the GRACE-C and model estimates from HWM14 and TIE-GCM. Two top panels show the daily mean and the daily standard deviation. Two bottom panels show the Pearson's correlation coefficient for TIE-GCM and HWM14, respectively, for two types of subsets: all data and low- to mid-latitudes. The values on the x-axis are common for all plots.

The mean density ratio (Sutton, 2018) was used for comparison

$$\mu(\rho_1, \rho_2) = \exp\left(\frac{1}{N}\sum_{n=1}^{N} \ln\frac{\rho_{1,n}}{\rho_{2,n}}\right), \tag{27}$$

where ρ_1/ρ_2 is the ratio between the observed and modelled density.

Fig. 16a shows the yearly mean of the observation-model density ratio. The solid lines represent the comparison between atmospheric models and version V2 (Siemes et al., 2023), whereas the dashed lines introduce version V2b, produced using new radiation pressure and thermal emission models. It can be seen that the ratio between the observations and DTM2020 is always larger than unity. This means that both previous and new observations consistently show a 5–10% higher density than the DTM2020 model. The only exception is 2021, where the annual mean increases to 25%. The observation-model ratio for NRLMSIS 2.0 is about 0.65 during the solar minimum

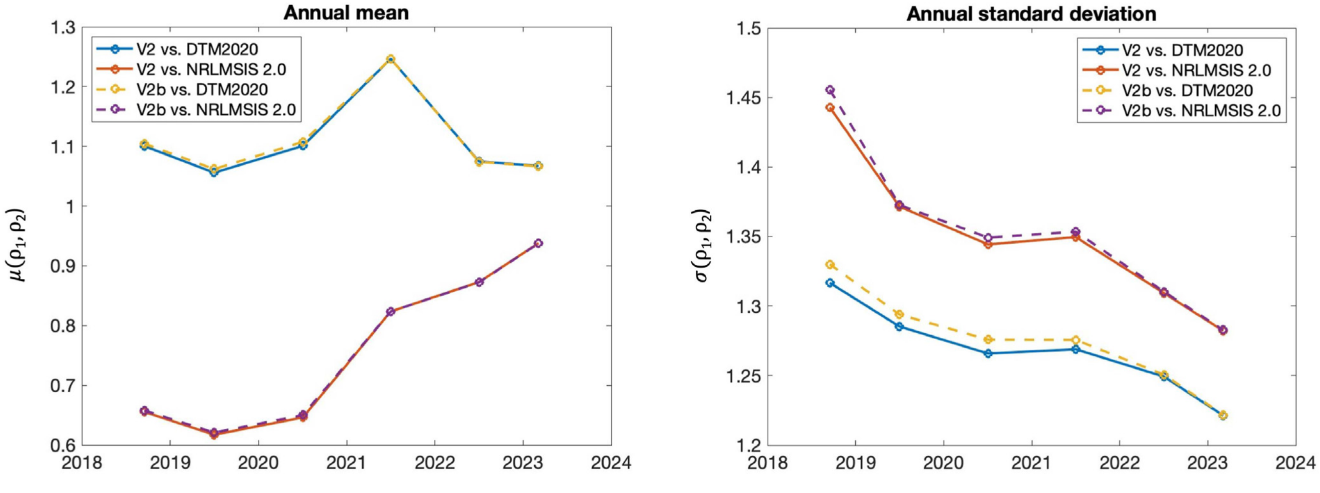

(a) GRACE-FO observation-model mean.

(b) GRACE-FO Observation-model standard deviation.

Fig. 16. Comparison of GRACE-FO density observations to DTM2020 and NRLMSIS 2.0. Observations of version V2 are based on Siemes et al. (2023) and V2b was developed wi.thin this study.

(2018–2020). This indicates the model's tendency to overestimate the density, which was already pointed out for Swarm data (van den IJssel et al., 2020). As solar activity increases from 2021 onward, the mean density ratio gets closer to one, indicating better agreement between observations and model during medium–high solar activity.

Comparison within versions does not show significant scale differences. This is expected since both V2 and V2b datasets share the same aerodynamic model and differ only in the radiation pressure and thermal emission, which average to zero in the yearly mean.

To compare the variability across the density data, the standard deviation of the density ratio was used:

$$\sigma(\rho_1,\rho_2)=\exp\left(\sqrt{\frac{1}{N-1}\sum_{n=1}^{N}\left(\ln\frac{\rho_{1,n}}{\rho_{2,n}}-\ln\mu(\rho_1,\rho_2)\right)^2}\right) \tag{28}$$

Fig. 16b shows the annual standard deviation. The annual standard deviations have continuously decreased since the beginning of the mission in 2018. This is likely caused by radiation pressure modelling errors playing a smaller role when the solar activity, and hence density, increases towards 2023. The annual standard deviation for DTM2020 is always lower compared to NRLMSIS 2.0, which indicates a better model agreement with observations' variability. Nevertheless, considerable values can still be seen for DTM2020, starting from 32% in 2018 to 22% in 2023. For NRLMSIS 2.0, the standard deviations range from 45% in 2018 to 28% in 2023. These larger values could be explained by the fact that the NRLMSIS 2.0 model is independent of the density observations produced after 2000.

Similarly to the annual mean, the standard deviations of V2 and V2b follow almost the same pattern. However, a small difference of about 1–2% can be spotted for the DTM2020 model. One may conclude that the V2b density observations are slightly worse. Yet, it is important to note that DTM2020 is based on the data where not all advances in radiation pressure modelling have been implemented. NRLMSIS 2.0 also indicates that the V2b data agrees less with the model, though the standard deviations are much larger than those of DTM2020, obscuring the subtle differences between V2 and V2b. Given the clear improvements in the crosswind observations, further investigation is needed to confirm if the changes in the variability of the V2b density data represent a worsening or improvement.

5. Conclusions and outlook

The motivation for this study was twofold: to determine the impact of radiation pressure and thermal emission modelling during periods of low solar activity and to derive updated density and crosswind datasets. The first was achieved by fine-tuning the reflection coefficients to characterise satellite surface properties better. A thermal emission model based on heat transfer was introduced together with the solar panel electric efficiency parameter. Achievements in radiation pressure modelling allowed for better cross-track calibration and improved crosswind datasets.

The accessibility of the thermistor measurements from the top and side panels was key to the success of this research. By knowing the external surface temperature, it was possible to disentangle the thermal emission from the other sources of radiation pressure and model it separately. To further improve the radiation pressure modelling accuracy, reliable data from thermistors in suitable locations on accelerometer-carrying satellites would be desired. Equipping future missions with thermistors that are distributed externally in multiple places would allow for an even more advanced modelling approach, for example, a finite-element thermal analysis. On the contrary, the inaccessibility of meaningful thermistor readings poses limitations on thermal emission modelling for past missions. This is the case for GRACE, where multiple temperature sensors were placed below the insulation foil, making a similar analysis as the one performed in this study meaningless since the thermistor data do not represent the topside temperature of the panel.

The thermal model accounting for thermal inertia significantly reduced the error compared to the instantaneous heat re-radiation. However, it is also more computationally demanding, as the calculations cannot be performed up-front but must be done along the orbit instead. Therefore, the choice of the appropriate thermal model depends on the required accuracy.

Taking into account the design similarities between GRACE-FO and Swarm solar arrays, it would be recommended to update the GRACE-FO documentation with the solar arrays' thermo-optical surface properties as specified for the Swarm mission. The surface coefficients defined for other materials should also be revisited. It was shown for the GRACE-FO apron, that in the case of foils, the reflection coefficients may vary depending on the wrinkling, and thus should be specified per separate foil sheet, and not globally for the whole material.

The improvements in the radiation pressure modelling did not have a significant impact on the density observations. In the case of the crosswind, a low aerodynamic signal along the track prevented the derivation of usable observations for some periods and manifested itself as spurious features in the crosswind data. To distinguish these spurious features from real geophysical signals, and to better attribute observation-model discrepancies, it would be beneficial to define reliable error bounds. Such error quantification should include errors in radiation pressure modelling, aerodynamic coefficient estimation, calibration errors and accelerometer measurement noise, as well as errors in external models providing thermosphere characteristics, such as uncertainty in the radiation fluxes and thermosphere composition. This work is currently in progress.

Declaration of Competing Interest

The authors declare that they have no known competing financial interests or personal relationships that could have appeared to influence the work reported in this paper.

Acknowledgments

The authors would like to thank Christopher Mccullough from NASA Jet Propulsion Laboratory for granting access to GRACE-FO thermistors data. An additional acknowledgement goes to Airbus Defence and Space for providing the CAD model of the GRACE-FO satellites and the information on the thermistors' location.

References

Barreto-Schuler, C.W., Shepherd, G.G., Chen, Y., et al., 2021. Observations and modeling of strong thermospheric winds at high latitudes and their impact on the lower thermosphere. J. Geophys. Res.: Space Phys. 126 (11). https://doi.org/10.1029/2021ja029658.

Bettadpur, S., 2012. Gravity recovery and climate experiment: Product specification document. Technical report GRACE 327–720 Center for Space Research. The University of Texas at Austin.

Bhattarai, S., Ziebart, M., Springer, T., et al., 2022. High-precision physics-based radiation force models for the Galileo spacecraft. Adv. Space Res. 69, 4141–4154. https://doi.org/10.1016/j.asr.2022.04.003.

Bruinsma, S., Boniface, C., 2021. The operational and research DTM-2020 thermosphere models. J. Space Weather Space Climate 11 (3). https://doi.org/10.1051/swsc/2021032.

Christophe, B., Boulanger, D., Foulon, B., et al., 2015. A new generation of ultra-sensitive electrostatic accelerometers for GRACE Follow-on and towards the next generation gravity missions. Acta Astronaut. 117, 1–7. https://doi.org/10.1016/j.actaastro.2015.06.021.

Doornbos, E., 2011. Thermospheric Density and Wind Determination From Satellite Dynamics. In: Department of Astrodynamics and Satellite Missions. Delft University of Technology.

Doornbos, E., Bruinsma, S., Fritsche, B., et al., 2014. ESA contract 4000102847/NL/EL, GOCE+ Theme 3: Air density and wind retrieval using GOCE data – Final Report. Technical Report TU Delft. URL: https://earth.esa.int/eogateway/documents/20142/1181177/GOCE-theme-3-final-report.pdf.

Doornbos, E., Scharroo, R., Klinkrad, H., et al., 2002. Improved modelling of surface forces in the orbit determination of ERS and ENVISAT. In: Technical Report Delft Institute for Earth-Oriented Space Research. Delft University of Technology Delft, Netherlands.

Doornbos, E., Van Den IJssel, J., Lühr, H., et al., 2010. Neutral density and crosswind determination from arbitrarily oriented multiaxis accelerometers on satellites. J. Spacecr. Rock. 47 (4), 580–589. https://doi.org/10.2514/1.48114.

Drob, D.P., Emmert, J.T., Crowley, G., et al., 2008. An empirical model of the Earth's horizontal wind fields: HWM07. J. Geophys. Res.: Space Phys. 113 (12). https://doi.org/10.1029/2008JA013668.

Drob, D.P., Emmert, J.T., Meriwether, J.W., et al., 2015. An update to the Horizontal Wind Model (HWM): The quiet time thermosphere. Earth Space Sci. 2 (7), 301–319. https://doi.org/10.1002/2014EA000089.

Duan, B., Hugentobler, U., 2022. Estimating surface optical properties and thermal thrust for Galileo satellite body and solar panels. GPS Solutions 26 (4). https://doi.org/10.1007/s10291-022-01324-1.

Fortescue, P., Swinerd, G., Stark, J., 2011. Spacecraft Systems Engineering, 4th Edition. Wiley, Chichester.

Gath, P. (2016). Entwicklung, Integration und Test der GRACE Follow-On Satelliten. Technical Report Airbus Defence and Space GmbH Friedrichshafen, Germany.

Harvey, N., McCullough, C.M., Save, H., 2022. Modeling GRACE-FO accelerometer data for the version 04 release. Adv. Space Res. 69 (3), 1393–1407. https://doi.org/10.1016/j.asr.2021.10.056.

van den IJssel, J., Doornbos, E., Iorfida, E., et al., 2020. Thermosphere densities derived from Swarm GPS observations. Adv. Space Res. 65 (7), 1758–1771. https://doi.org/10.1016/j.asr.2020.01.004.

Kenneally, P.W., Schaub, H., 2020. Fast spacecraft solar radiation pressure modeling by ray tracing on graphics processing unit. Adv. Space Res. 65, 1951–1964. https://doi.org/10.1016/j.asr.2019.12.028.

Killeen, T.L., Roble, R.G., 1984. An analysis of the high-latitude thermospheric wind pattern calculated by a thermospheric general circulation model: 1. momentum forcing. J. Geophys. Res.: Space 89 (A9), 7509–7522. https://doi.org/10.1029/ja089ia09p07509.

Klinkrad, H., Koeck, C., Renard, P., 1991. Key features of a satellite skin force modelling technique by means of monte-carlo ray tracing. Adv. Space Res. 11 (6), 147–150. https://doi.org/10.1016/0273-1177(91)90244-E.

Kodikara, T., 2023. The open time-series of the high-resolution ionosphere-thermosphere aeronomic climate simulation (OTHITACS). In: World Data Center for Climate (WDCC) at DKRZ. https://doi.org/10.26050/WDCC/OTHITACS_TIEGCM.

Kornfeld, R.P., Arnold, B.W., Gross, M.A. et al. (2019). GRACE-FO: The gravity recovery and climate experiment follow-on mission. In Journal of Spacecraft and Rockets (pp. 931–951). AIAA International volume 56. doi:10.2514/1.A34326.

Kraft, 1988. A software package for sequential quadratic programming. Tech. Rep. DFVLR-FB 88–28, DLR German Aerospace Center — Institute for Flight Mechanics, Koln, Germany. Wiss. Berichtswesen d. DFVLR, 1988, URL: https://books.google.nl/books?id=4rKaGwAACAAJ.

Landerer, F.W., Flechtner, F.M., Save, H., et al., 2020. Extending the Global Mass Change Data Record: GRACE Follow-On Instrument and Science Data Performance. Geophys. Res. Lett. 47 (12). https://doi.org/10.1029/2020GL088306.

Li, Z., Ziebart, M., Bhattarai, S., et al., 2018. Fast solar radiation pressure modelling with ray tracing and multiple reflections. Adv. Space Res. 61 (9), 2352–2365. https://doi.org/10.1016/J.ASR.2018.02.019.

Lühr, H., Park, J., Ritter, P., et al., 2011. In-situ CHAMP observation of ionosphere-thermosphere coupling. Space Sci. Rev. 168 (1–4), 237–260. https://doi.org/10.1007/s11214-011-9798-4.

Lühr, H., Rentzl, S., Ritter, P., et al., 2007. Average thermospheric wind patterns over the polar regions, as observed by CHAMP. Ann. Geophys. 25, 1093–1101. https://doi.org/10.5194/angeo-25-1093-2007.

March, G., Doornbos, E.N., Visser, P.N., 2019. High-fidelity geometry models for improving the consistency of CHAMP, GRACE, GOCE and Swarm thermospheric density data sets. Adv. Space Res. 63 (1), 213–238. https://doi.org/10.1016/j.asr.2018.07.009.

Montenbruck, O., Steigenberger, P., Hugentobler, U., 2015. Enhanced solar radiation pressure modeling for Galileo satellites. J. Geodesy 89 (3), 283–297. https://doi.org/10.1007/s00190-014-0774-0.

Picone, J.M., Hedin, A.E., Drob, D.P., et al., 2002a. NRLMSISE-00 empirical model of the atmosphere: Statistical comparisons and scientific issues. J. Geophys. Res.: Space Phys. 107 (A12). https://doi.org/10.1029/2002JA009430.

Picone, J.M., Hedin, A.E., Drob, D.P. et al., 2002b. NRLMSISE-00 empirical model of the atmosphere: Statistical comparisons and scientific issues. J. Geophys. Res.: Space Phys., 107(A12)(1468). doi:10.1029/2002JA009430.

Richmond, A.D., Lathuillère, C., Vennerstroem, S., 2003. Winds in the high-latitude lower thermosphere: Dependence on the interplanetary magnetic field. J. Geophys. Res.: Space Phys. 108 (A2). https://doi.org/10.1029/2002ja009493.

Richmond, A.D., Ridley, E.C., Roble, R.G., 1992. A thermosphere/ionosphere general circulation model with coupled electrodynamics. Geophys. Res. Lett. 19 (6), 601–604. https://doi.org/10.1029/92GL00401.

Robertson, R.V., Earle, G.D., Bailey, S.M., et al., 2015. Highly Physical Solar Radiation Pressure Modeling During Penumbra Transitions Ph. D. thesis. Virginia Polytechnic Institute and State University Virginia, United States.

Siemes, C., 2019. ESA UNCLASSIFIED-Releasable to the Public Title Swarm satellite thermo-optical properties and external geometry Issue Number 2 Revision Number 0. Technical Report Delft University of Technology Delft, Netherlands.

Siemes, C., Borries, C., Bruinsma, S., et al., 2023. New thermosphere neutral mass density and crosswind datasets from CHAMP, GRACE, and GRACE-FO. J. Space Weather Space Climate 13, 16. https://doi.org/10.1051/swsc/2023014.

Sutton, E.K., 2018. A new method of physics-based data assimilation for the quiet and disturbed thermosphere. Space Weather 16, 736–753. https://doi.org/10.1002/2017SW001785.

Tapley, B.D., Bettadpur, S., Watkins, M., et al., 2004. The gravity recovery and climate experiment: Mission overview and early results. Geophys. Res. Lett. 31 (9). https://doi.org/10.1029/2004GL019920.

Vielberg, K., Kusche, J., 2020. Extended forward and inverse modeling of radiation pressure accelerations for LEO satellites. J. Geodesy 94 (4). https://doi.org/10.1007/s00190-020-01368-6.

Wang, Y., Li, M., Jiang, K., et al., 2023. Improving Precise Orbit Determination of LEO Satellites Using Enhanced Solar Radiation Pressure Modeling. Space Weather 21 (1). https://doi.org/10.1029/2022SW003292.

Wöske, F., Kato, T., Rievers, B., et al., 2019. GRACE accelerometer calibration by high precision non-gravitational force modeling. Adv. Space Res. 63 (3), 1318–1335. https://doi.org/10.1016/j.asr.2018.10.025.

Ying, H., Kruizinga, W.G., Paik, M. et al., 2019. Gravity Recovery and Climate Experiment Follow-On (GRACE-FO) Level-1 Data Product User Handbook Revision History. Technical Report NASA Jet Propulsion Laboratory, California Institute of Technology.

Ziebart, M., 2004. Generalized analytical solar radiation pressure modeling algorithm for spacecraft of complex shape. J. Spacecr. Rock. 41 (5), 840–848. https://doi.org/10.2514/1.13097.